A&A 534, A43 (2011)
DOI: 10.1051/0004-6361/201116898


Astronomy & Astrophysics

# Photometric selection of Type Ia supernovae in the Supernova Legacy Survey

G. Bazin[1,17], V. Ruhlmann-Kleider[1], N. Palanque-Delabrouille[1], J. Rich[1], E. Aubourg[1], P. Astier[2], C. Balland[2,3], S. Basa[4], R. G. Carlberg[5], A. Conley[6], D. Fouchez[7], J. Guy[2], D. Hardin[2], I. M. Hook[8,9], D. A. Howell[10,11], R. Pain[2], K. Perrett[5,12], C. J. Pritchet[13], N. Regnault[2], M. Sullivan[8], N. Fourmanoit[2], S. González-Gaitán[5], C. Lidman[14], S. Perlmutter[15], P. Ripoche[15,2], and E. S. Walker[8,16]

[1] CEA, Centre de Saclay, Irfu/SPP, 91191 Gif-sur-Yvette, France
[2] LPNHE, Université Pierre et Marie Curie, Université Paris Diderot, CNRS-IN2P3, 4 place Jussieu, 75252 Paris Cedex 05, France
[3] University Paris 11, 91405 Orsay, France
[4] LAM, CNRS-INSU, BP 8, Pôle de l'étoile, Site de Château-Gombert, 38 rue Frédéric Joliot-Curie, 13388 Marseille Cedex 13, France
[5] Deparment of Astronomy and Astrophysics, University of Toronto, 50 St. George Street, Toronto, ON M5S 3H8, Canada
[6] Center for Astrophysics and Space Astronomy, University of Colorado, Boulder, CO 80309-0389, USA
[7] CPPM, CNRS-Luminy, Case 907, 13288 Marseille Cedex 9, France
[8] Department of Physics (Astrophysics), University of Oxford, Denys Wilkinson Building, Keble Road, Oxford OX1 3RH, UK
[9] INAF – Osservatorio Astronomico di Roma, via Frascati 33, 00040 Monteporzio (RM), Italy
[10] Las Cumbres Observatory Global Telescope Network, 6740 Cortona Dr., Suite 102, Goleta, CA 93117, USA
[11] Department of Physics, University of California, Santa Barbara, Broida Hall, Mail Code 9530, Santa Barbara, CA 93106-9530, USA
[12] Network Information Operations, DRDC-Ottawa, 3701 Carling Avenue, Ottawa, ON, K1A 0Z4, Canada
[13] Department of Physics and Astronomy, University of Victoria, PO Box 3055, Victoria, BC V8W 3P6, Canada
[14] Australian Astronomical Observatory, PO Box 296, Epping, NSW 1710, Australia
[15] LBNL, 1 Cyclotron Rd, Berkeley, CA 94720, USA
[16] Scuola Normale Superiore, Piazza des Cavalieri 7, 56126 Pisa, Italy
[17] Department of Physics, Ludwig-Maximilians-Universität, Scheinerstr. 1, 81679 München and Excellence Cluster Universe, Boltzmannstr. 2, 85748 Garchhing, Germany

Received 16 March 2011 / Accepted 23 August 2011

**ABSTRACT**

We present a sample of 485 photometrically identified Type Ia supernova candidates mined from the first three years of data of the CFHT SuperNova Legacy Survey (SNLS). The images were submitted to a deferred processing independent of the SNLS real-time detection pipeline. Light curves of all transient events were reconstructed in the $g_M$, $r_M$, $i_M$ and $z_M$ filters and submitted to automated sequential cuts in order to identify possible supernovae. Pure noise and long-term variable events were rejected by light curve shape criteria. Type Ia supernova identification relied on event characteristics fitted to their light curves assuming the events to be normal SNe Ia. The light curve fitter SALT2 was used for this purpose, assigning host galaxy photometric redshifts to the tested events. The selected sample of 485 candidates is one magnitude deeper than that allowed by the SNLS spectroscopic identification. The contamination by supernovae of other types is estimated to be 4%. Testing Hubble diagram residuals with this enlarged sample allows us to measure the Malmquist bias due to spectroscopic selections directly. The result is fully consistent with the precise Monte Carlo based estimate used to correct SN Ia distance moduli in the SNLS 3-year cosmological analyses. This paper demonstrates the feasibility of a photometric selection of high redshift supernovae with known host galaxy redshifts, opening interesting prospects for cosmological analyses from future large photometric SN Ia surveys.

**Key words.** supernovae: general – cosmology: observations

## 1. Introduction

The accelerated expansion of the Universe was revealed by studies of high redshift Type Ia supernovae (SNe Ia) (Riess et al. 1998; Perlmutter et al. 1999). Since then, second-generation experiments with efficient observation strategies were set up to achieve more precise cosmological measurements from SNe Ia, such as the SNLS (Astier et al. 2006), ESSENCE (Miknaitis et al. 2007) and SDSS-II Supernova Survey projects (Frieman et al. 2008). In order to meet the precision required by such measurements, samples of SNe Ia rely on photometry to detect transient events and to measure their light curves, while SN Ia types and redshifts are provided by follow-up spectroscopy. In this paper, we describe a method based on photometry alone to detect and select supernova candidates, assigning them galaxy photometric redshifts from an external catalogue. This method was applied in a deferred analysis of the first three years of the Supernova Legacy Survey (SNLS) conducted at the Canada-France-Hawaii Telescope (CFHT) from 2003 to 2008, as part of the Deep Synoptic Survey of the CFHT Legacy Survey (CFHT-LS).

SNLS was defined with an optimised observing strategy. Four one-square degree fields were targeted throughout the 5 to 7 consecutive lunations where they remained visible. In every

lunation, each visible field was repeatedly observed every 3 or 4 nights during dark time. This rolling-search mode allowed supernova light curves to be measured with very good time sampling in four broadband filters, denoted $g_M$, $r_M$, $i_M$ and $z_M$, similar to the SDSS filter set (Regnault et al. 2009) and spanning the wavelength range from 400 to 1000 nm. These measurements were made with the MegaCam imager (Boulade et al. 2003), a 1 square degree array of 36 CCDs with 340 million pixels in total.

The standard SN Ia selection for the SNLS cosmological analyses, based on real-time detection (Perrett et al. 2010) and follow-up spectroscopy can be found in Astier et al. (2006) for the first year data sample and in Guy et al. (2010) for the 3-year sample. Spectral data from the SNLS follow-up spectroscopy are described in Howell et al. (2005), Bronder et al. (2008), Ellis et al. (2008), Balland et al. (2009) and Walker et al. (2010). Photometric selections are commonly used in SNLS to define spectroscopic follow-up prioritisation from real-time (and thus partial) light curves (Sullivan et al. 2006a) or to enlarge the real-time SN Ia sample in order to measure SN Ia rates or properties (Sullivan et al. 2006b). Photometric SN classification is also expected to become a key challenge for future supernova projects by lack of spectroscopic resources to confirm the large amount of supernovae that will be detected (Kessler et al. 2010).

The photometric analysis described in this paper is independent from the SNLS real-time detection pipeline and the ensuing cosmological analyses. It uses different data processing and detection, and applies a coherent set of cuts on 3-year light curves of all detected events, whether with or without spectroscopic information. Benefitting from more complete light curves and less stringent minimal brightness constraints than the real-time spectroscopic selection, the photometric analysis aims at going deeper in magnitude. As such, it can provide a cross-check to estimate possible biases of the standard SNLS SN Ia selection for cosmological analyses. It is also the basis of a photometric selection of non-Type Ia supernovae that allowed the core-collapse supernova rate to be measured at a mean redshift $z \sim 0.3$ (Bazin et al. 2009). Ultimately, it aims at exploring the feasibility of a cosmological analysis with a photometric SN Ia sample, which will be the subject of a future paper.

The outline of the paper is as follows. Data processing, transient event detection and photometry are described in Sect. 2. The selection of SN-like transient events and their association with host galaxy photometric redshifts are presented in Sect. 3. The selection of SN Ia candidates is discussed in Sect. 4. The characteristics of the SN Ia candidates are presented in Sect. 5 where selected events with and without spectroscopic identification are compared in the same range of magnitude and found to have similar properties. Finally, distance estimates from the whole photometric sample and from the subsample with spectroscopic identification, which has a lower limiting magnitude, are compared in Sect. 5.2.

## 2. Detection and photometry

### 2.1. Transient event detection

Data corresponding to SNLS observations from March 1st, 2003 to September 21th, 2006 were analysed, using images preprocessed at the end of each lunation with the Elixir pipeline at CFHT (Magnier & Cuillandre 2004) which provided flat-fielding and fringe subtraction. These data include the presurvey period (up to June 1st, 2003) which was used for the commissioning of MegaCam and thus corresponds to unstable observing conditions.

The astrometric solution for the images of each of the four SNLS fields (D1, D2 , D3 and D4) was computed with the TERAPIX[1] calibration tool SCAMP (Bertin 2006) and the USNO-B1.0 catalogue (Monet et al. 2003). The images were then resampled with the TERAPIX tool SWarp (Bertin et al. 2002) according to the previously determined astrometric solution. A set of about 20 images with the best photometric quality (based on seeing and absorption considerations) was selected for each field and each filter ($g_M$, $r_M$, $i_M$ or $z_M$) and co-added with SWarp in order to define reference images. The selected images were all chosen in the first or second season, depending on the field. The same reference images were used throughout the processing.

Cosmic rays, defects due to dead pixels or induced by the resampling procedure were searched for in the resampled images and in the reference images. The content of the corresponding pixels was replaced by the estimate of the local sky background. An image subtraction package, TRITON (Leguillou 2003), based on the algorithm of Alard & Lupton (1998), was then applied on every resampled image. In this procedure, the convolution kernel and the sky background were determined independently on eight identical non-overlapping tiles paving each CCD of the mosaic. The number of tiles was chosen to optimise the precision of the subtractions, spatial variations of the kernel and sky background requiring small tiles, whereas the kernel determination requires a sufficient number of bright objects and thus large tiles. To select bright objects to be used in the convolution kernel determination for a given tile, the TERAPIX tool SExtractor (Bertin et Arnouts 1996) was applied to both the reference and the current images, with a detection threshold at $2\sigma$ w.r.t. sky background. Bright objects present in both selections and neither saturated nor too close to a tile boundary were kept, which left about 100 objects per tile for images at the average seeing of 0.7 arcsec. The kernel and sky background were then fitted in $59 \times 59$ pixel regions centred on each object. Adjacent objects whose signal regions were overlapping by more than 20% were discarded. Subtractions were considered as valid only if the integral of the convolution kernel was found to be above a filter-dependent threshold. The rate of lost subtractions (either failed or not valid) was around a few %.

In each field, subtracted images in the $i_M$ filter were stacked for each lunation. On average, 27 images entered each stack. SExtractor was applied on each stack to construct catalogues of objects exhibiting a variable flux – whether positive or negative – in the $i_M$ filter in any lunation. At least 4 adjacent pixels with a signal of more than $2.5\sigma$ w.r.t. sky background were required to confirm an object. As the same set of reference images was kept throughout the whole processing, some supernovae may have part of their signal included in the references. In that case, the events might appear as missing flux on each of the images and could have been missed if searching only for a flux excess. Considering negative measured fluxes when building the above catalogues allowed us to recover those events.

All lunation catalogues were then merged to produce the final detection map. In this way, any object detected on several lunations gave only one detection, with a position averaged over all lunation stacks.

When applied to the 3-year data sample of SNLS, the above detection pipeline produced a total of about 300 000 detections,

[1] See http://www.astromatic.net/software for the TERAPIX software.

dominated mostly by saturated signals from bright objects which were not perfectly subtracted. The efficiency of the pipeline is discussed in the next section, while photometry is described in Sect. 2.3 and further selections to discriminate between spurious detections and supernova signals are the subject of Sect. 3.

### 2.2. Detection efficiency

In order to check the performance of the above pipeline, we studied the detection efficiency with Monte Carlo generated artificial images produced for the D1 field in the $i_M$ filter that we used for the detection. From this study we derived an efficiency model that allowed us to determine the efficiency for the other fields, D2, D3 and D4, which had slightly different mean observing conditions. This efficiency model was then coupled with a simulation of synthetic light curves (described in Sect. 3.3.1) that we set up to study our photometric selection criteria.

The D1 Monte Carlo images were obtained by adding 216 000 simulated supernovae to real images, thus naturally reproducing the observing conditions (sampling frequencies and photometric quality) of the experiment (Ripoche 2007). An external catalogue of host galaxies identified from deep image stacks of the CFHT-LS Deep Fields (Ilbert et al. 2006) was used to randomly choose the position of each simulated supernova, following the observed surface brightness of the hosts, and to set the redshift, equal to the photometric redshift of the host. The redshift was restricted to the range between 0.2 and 1.2. The supernovae were attributed a random stretch, colour and intrinsic dispersion term according to the distributions observed with spectroscopically identified SNe Ia. The time of maximum luminosity was drawn uniformly within each roughly six-month long season of observation. The $i_M$-band light curve of each artificial supernova was computed using SALT2 (Guy et al. 2007) and the supernova flux at each observation date as deduced from the light curve was added to the corresponding images. The images were then processed with the same pipeline as the real images, setting the backgrounds and convolution kernels to those measured on the original images in order to avoid biases in the subtraction procedure due to the presence of the numerous simulated supernovae. The detection efficiency was then defined as the fraction of simulated supernovae recovered in the detection map at the end of the processing.

The detection efficiency for a supernova with date $t_{0i}$ of maximum light in $i_M$-band depends on its peak magnitude $m_{0i}$, on the seeing and sky background during nearby observing times $t_k$, and on the relative epochs $t_{0i} - t_k$. The Monte Carlo images allowed us to study the efficiency dependence on these variables, in order to build an efficiency model to extrapolate from D1 to the other fields. As an example, the average first season detection efficiency, $\epsilon(m_{0i})$ is illustrated in Fig. 1 for D1. The efficiency is rather uniform over the CCD mosaic, except for CCD 3 which failed to work during three out of the six dark time periods of the first season. The efficiency is nearly magnitude-independent, $\epsilon_{\max} \sim 0.97$, out to $m_{0i} = 23.5$ in the SNLS magnitude system[2]. This is followed with a steep decline at faint magnitudes reaching an efficiency of 0.50 at $m_{0i} \sim 24.7$. Very similar efficiencies were obtained in the other two seasons. Figure 1 also shows the result of our efficiency model that reproduces the dependence of the efficiency as a function of the SN Ia peak magnitude. This model is described in Appendix A.

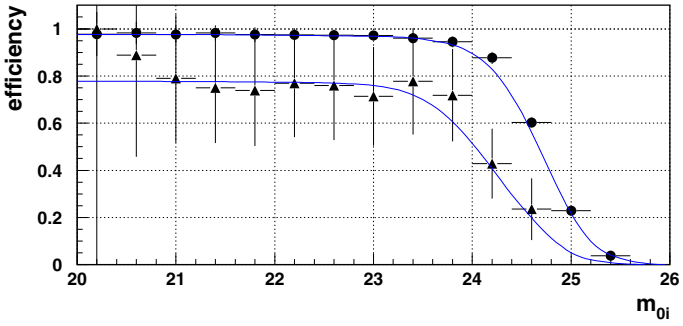


**Fig. 1.** Detection efficiency $\epsilon(m_{0i})$ for the first season of D1 as a function of the generated peak magnitude in $i_M$. The model (blue curve) is compared with Monte Carlo estimates (symbols), showing separately the efficiency for CCD 3 (triangles), or averaged over the rest of the mosaic (dots).

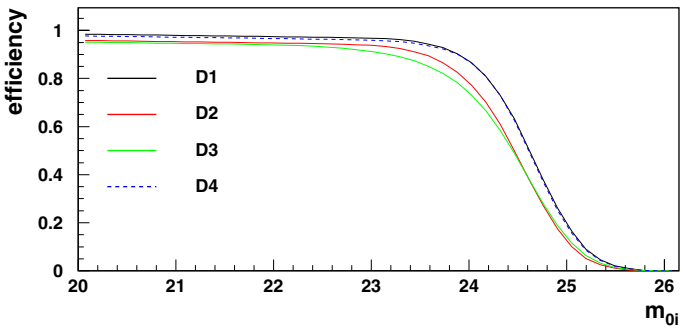


**Fig. 2.** Detection efficiency averaged over the entire CCD mosaic for fields D1, D2, D3 and D4 as a function of the generated peak magnitude in $i_M$.

The efficiency model was applied to fields D2, D3 and D4, using the observation dates on these fields and the information of seeing and background for each exposure. Each CCD was treated independently to reproduce exactly the possible failures, whether electronic or due to the processing of the real images. The detection efficiency computed for each field over the observing period between March 2003 and September 2006 and averaged over the entire mosaic is shown in Fig. 2. Fields D2 and D3 have a smaller efficiency than D1 and D4. This is caused by the lack of data due to bad weather in February 2004 and in March 2006, when only D2 and D3 were observable.

### 2.3. Photometry and calibration

For each of the 300 000 detections, four-filter light curves were built from individual subtracted images. TRITON differential photometry with Point Spread Function (PSF) fitting was applied, imposing the position found in the $i_M$ detection map (see Sect. 2.1). Fluxes were normalised by the integral of the convolution kernel determined in the subtractions, in order to express all fluxes on a common scale, that of the reference image. For each exposure and CCD, the PSF was determined as follows. Bright events were first detected on each resampled image using SExtractor. The flux in the pixel of maximum content and the integrated flux of the event allowed saturated stars and galaxies to be identified and rejected. This left about 100 non saturated stars in each CCD, which were used to define one PSF per CCD by averaging the star profiles computed in a seeing-dependent box.

[2] The SNLS magnitude system uses star BD +17 4708 as a flux standard, which, as compared with the standard reference Vega, has the advantage of known Landolt magnitudes, precise SED measurements and colours close to the avergae colours of the Landolt stars used in the SNLS calibration (Regnault et al. 2009).

The measured fluxes were calibrated using the SNLS tertiary standards published in Regnault et al. (2009). We measured the tertiary star fluxes directly on current images with the same photometry algorithm and PSF as for transient events and, as for the latter, the star fluxes were normalised by the convolution kernel integral determined in the subtractions. Using the magnitudes published in Regnault et al. (2009), the tertiary star fluxes were then converted into zero-points for each exposure and a weighted average of these zero-points was computed over each CCD, rejecting zero-points above $5\sigma$ w.r.t. the median value. The measured star fluxes were compared with fluxes derived from the star magnitudes by applying the average zero-points and the relative flux difference was fitted as a function of flux (assuming a linear variation). In the whole range of tertiary star fluxes, the fitted relative flux difference was found to remain below 0.3% whatever the field or band. Note that Regnault et al. (2009) also provides flat-fielding corrections due to residual radial non-uniformities of the imager photometric response. These corrections were applied to all measured fluxes, prior to any further treatment (conversion into zero-point for stars or calibration for transient events).

The calibrated fluxes were then filtered. Residual defects from bad pixels or cosmic rays, detections due to satellite trails or saturated stars were identified on subtracted images as bright objects selected by SExtractor with a detection threshold at $3\sigma$ w.r.t. sky background. Photometric points whose PSF overlapped the spatial extension of any of the above objects were discarded. Flux measurements obtained under bad seeing conditions (above 1.2″) were also eliminated, as well as flux measurements in nights where all exposures were of bad quality[3]. At this point, flux errors were renormalised so that after filtering the distribution of the pulls of the exposure fluxes w.r.t. the night flux average be of variance 1 in the test-sample of 278 light curves matched to spectroscopically identified SNe Ia in our detections (see Sect. 3.2). Then, in any light curve, points with flux errors either too low (w.r.t. the expected flux uncertainty due to sky background) or too high were discarded. Only exposures with a flux within $3\sigma$ from the night flux median value were retained and only nights with at least two such exposures were kept. On average over all reconstructed light curves, the fraction of measurements removed by the above cuts is at most 15%.

Flux measurements corresponding to selected exposures within the same night were weighted by their errors and averaged to define mean light curves in each of the four filters. Finally, in order to account for a possible contribution of variable objects in the reference images, a common baseline, defined as the mode of the flux distribution, was computed in each mean light curve and then withdrawn from the latter.

The flux estimation was checked with the set of 278 spectroscopically identified SNe Ia previously mentioned. Peak magnitudes at the date of $B$-band maximum light from our light curves were compared with those derived from the SNLS-3 year light curves published in Guy et al. (2010) which correspond to a different image processing and an optimised photometry. In order to restrict to light curves of good quality, both sets were submitted to sampling and S/N cuts as described in Guy et al. (2010). The selected light curves were then fitted with SALT2 in each filter fixing the date of $B$-band maximum light, $X_1$ and colour at the values obtained from a multi-band fit to the SNLS-3 year light curves (see Sect. 2.5). Only photometric points present in both sets of light curves were considered in the fits.

**Table 1.** Performance of the photometry used in this work.

| Band | Full sample | | Optimal conditions | |
|---|---|---|---|---|
| | Median | MAD | Median | MAD |
| $g_M$ | 0.006 | 0.016 | –0.0001 | 0.014 |
| $r_M$ | 0.018 | 0.028 | 0.006 | 0.020 |
| $i_M$ | 0.015 | 0.023 | 0.001 | 0.016 |
| $z_M$ | 0.009 | 0.054 | –0.002 | 0.047 |

**Notes.** The table shows the difference $m_1 - m_2$ of the SALT2 fitted peak magnitudes obtained with the photometry of this paper ($m_1$) and with the SNLS-3 year photometry ($m_2$): median magnitude difference and median absolute dispersion (MAD) for all SNe Ia with good quality light curves (left) and for the subset detected in optimal conditions, as described in the text (right).

Differences in the peak magnitudes fitted in each band are summarised in the left-hand column in Table 1. Magnitudes from our light curves are fainter by at most 0.02 mag with dispersions between 0.02 and 0.05 mag. Two effects explain these differences. Some of the SNe had SN light included in our reference images, which had no impact on their detection but affected their photometry. Second, even for SNe with no light in the reference images, the magnitude difference was observed to be larger when the SN was located near the top or bottom edges of the mosaic. Restricting to SNe with no light in the reference images and located far from the top/bottom mosaic borders, closer performance between the two photometry techniques are obtained, as shown in the right-hand column in Table 1 (column labelled "optimal conditions").

The dependence of the magnitude difference with the SN location is likely to be due to our using the position found in the $i_M$ detection stack as the pivot of the PSF photometry. This is not optimal, especially on image edges due to distortions induced by alignment which are expected to be more important there. The average $i_M$ position resolution provided by our detection pipeline was found to be 0.41 pixel in the full sample of SNe Ia and 0.32 pixel for SNe in optimal conditions, to be compared with 0.28 pixel in the photometry of Guy et al. (2010) which performs a simultaneous fit of SN Ia positions and fluxes[4]. Position measurement inaccuracy leads to underestimated fluxes. Using Appendix B of Guy et al. (2010), we found that resolutions of 0.41, 0.32 and 0.28 pixel would lead on average to $i_M$ biases of 0.011, 0.007 and 0.005 mag, respectively. These numbers reproduce the order of magnitude of the effect reported in Table 1.

Summarising, when all SNe are considered, fluxes in this analysis are reconstructed with resolutions of a few % and an uncertainty below 2% on the absolute flux scale, which is accurate enough to set up a photometric selection.

### 2.4. Catalogue of stars and galaxies

The analysis described in this paper uses a catalogue of nearly 2 million stars and galaxies present in the four SNLS fields. It combines two sources. The first one, published in Ilbert et al. (2006), provides positions of stars and galaxies, as well as photometric redshifts for the latter. The second was obtained by applying SExtractor on our reference images and contains measurements of the object size. The two catalogues were combined

[3] Grade C from the TERAPIX visual image quality control as found in the TERAPIX Spica database, http://clix.iap.fr/steeringgroup/qf/

[4] Note that this procedure is ideal when a limited number of objects is to be reconstructed but would be too time consuming when dealing with all transient events detected by our photometric pipeline.

into one. Events common to both catalogues were classified as star or galaxy based on their classification in each of the catalogues. Ambiguous cases of star vs galaxy classification (e.g. at fainter magnitudes) were solved with the help of flux and size measurements from our reference images. Altogether, the catalogue consists of 94% galaxies, 5% stars and only 1% ambiguous objects.

The Ilbert et al. (2006) catalogue also provides photometric redshifts for more than 520 000 galaxies with an AB magnitude brighter than 25 in $i_M$. The photometric redshift method was applied to the CFHT-LS multi-colour data of the four deep fields of the survey. It was trained with around 3000 VVDS spectra observed with VIMOS in one of the CFHT-LS deep fields, in both visible and near infrared bands. The method reaches a redshift resolution of 0.037 with 3.7% of catastrophic redshift errors for a sample selected at $i_M \leq 24$. All galaxy photometric redshifts used in the following are from this catalogue.

### 2.5. Light curve fitter

Throughout this paper, we use the SALT2 package as a SN Ia light curve fitter. The version is that described in Guy et al. (2010) which was trained on a larger data sample and has a higher resolution colour variation law than the original version of Guy et al. (2007). SALT2 models the mean evolution of the spectral energy distribution sequence of SNe Ia. The model was trained on Branch-normal supernova data, both multi-band light curves and spectra, covering low and high redshifts up to 0.7. The resulting flux model of a SN Ia at a given redshift is a function of four parameters. Those are the $B$-band global flux normalisation factor, $X_0$, the date of $B$-band maximum light and two intrinsic rest-frame parameters, a stretch-related parameter, $X_1$ and a colour parameter, defined as the $(B-V)$ colour offset at the date of $B$-band maximum light with respect to the average colour in the training sample, $C = (B-V)_{\max} - \langle B-V \rangle$.

In this paper, SALT2 was used either to produce synthetic SN Ia light curves assuming a given cosmology or to fit observed light curves under the assumption that they come from a SN Ia. In that case, the results are magnitudes, either in the MegaCam filters or in the rest-frame $B$-band. Except in Sect. 2.3, these magnitudes are estimated from a global fit to photometric points in all filters that are expected to provide a significant contribution at the event redshift.

## 3. Supernova selection

First, we apply a set of selection criteria to the light curves of all candidate detections in order to reject spurious objects and select for SN-like events. The SN selection criteria, described in the next section, were designed to be efficient for all types of supernovae. Spectroscopically identified supernovae present in our sample (see Sect. 3.2) and synthetic SN Ia light curves (see Sect. 3.3) were used as qualitative guidelines to define the cuts.

### 3.1. Selection criteria

The selection proceeds in four steps. The light curves were first searched for a significant flux variation in order to select variable objects. We then checked that the main variation in each curve had a shape consistent with that expected from a SN event and that there was no other flux variation away from the SN-like variation. Events likely due to stars were then removed. Eventually, sampling requirements were applied to ensure good quality light curves were selected. These four steps are detailed below.

#### 3.1.1. Search for flux variations

In each light curve and filter, a search for significant flux variations was applied. Variations were due to start with a photometric point of positive flux and significance above $1\sigma$. They ended if a point of negative flux had a significance above $1\sigma$, if two successive points of positive fluxes had significances below $1\sigma$ or at season ends, since supernovae are expected to show only short-term variations lasting typically over three consecutive lunations. To reduce the amount of spurious detections, the most significant variations found in the $i_M$ and $r_M$ light curves were required to contain each at least three points and to have their dates of maximum flux within 50 days from one another. This reduced the number of detections by about a factor 6.

#### 3.1.2. SN-like variation

Most events at this stage were either spurious detections or objects varying on a longer term than supernovae. To be considered further, light curves were then required to have a shape compatible with that of SN-like events. To test this, the main variation in each filter was fitted with the phenomenological form:

$$f^k(t) = A^k \frac{e^{-(t-t_0^k)/\tau_{\rm fall}^k}}{1+e^{-(t-t_0^k)/\tau_{\rm rise}^k}} + c^k \quad (1)$$

where $k$ indicates the filter. Besides a constant, $c^k$, the fit parameters are $A^k$, which sets the normalisation of the variable signal, $\tau_{\rm fall}^k$ and $\tau_{\rm rise}^k$, which define the fall and rise times of the variation, respectively, and $t_0^k$ which is related to the date of maximum by $t_{\max}^k = t_0^k + \tau_{\rm rise}^k \ln(\tau_{\rm fall}^k/\tau_{\rm rise}^k - 1)$. Fits were independent in the four bands and run over the entire 3-year light curves. While form 1 has no particular physical motivation, it is sufficiently general to fit the light curve shape of all types of supernovae.

To reduce the contamination by long-term variable objects or by random fluctuations, we first required that points away from the main variation were compatible with a constant flux. To do so, points outside the time interval of the main variation in $i_M$ were compared with the constant from the previous fit. Their significances w.r.t. that constant were added in quadrature over all four filters and the sum was normalised to the total number of points in the sum. This defined the following variable, hereafter referred as to off-variation $\chi^2$:

$$\chi^2_{\rm off} = \frac{1}{\sum_k N_k} \sum_k \sum_{j \notin \rm var} \left( \frac{F_j^k - c^k}{\sigma_j^k} \right)^2$$

where $k$ indicates the filter and $F_j$ represents the flux as measured at point $j$ in the light curve with an error $\sigma_j$. A cut was applied on $\chi^2_{\rm off}$ as a function of the maximum flux observed in $i_M$. As a result, about half of the detections resulted in light curves which, outside the main variation, were more irregular than those of SNe.

The shape of the light curve was then tested for consistency with (1). This was done in the $i_M$ filter only, as a significant signal is expected in this filter at all redshifts and for all types of SNe. A cut was applied on the difference in reduced $\chi^2$ between a fit by a constant and the fit by formula (1), as a function of the reduced $\chi^2$ of the latter fit. This cut is illustrated in Fig. 3 where

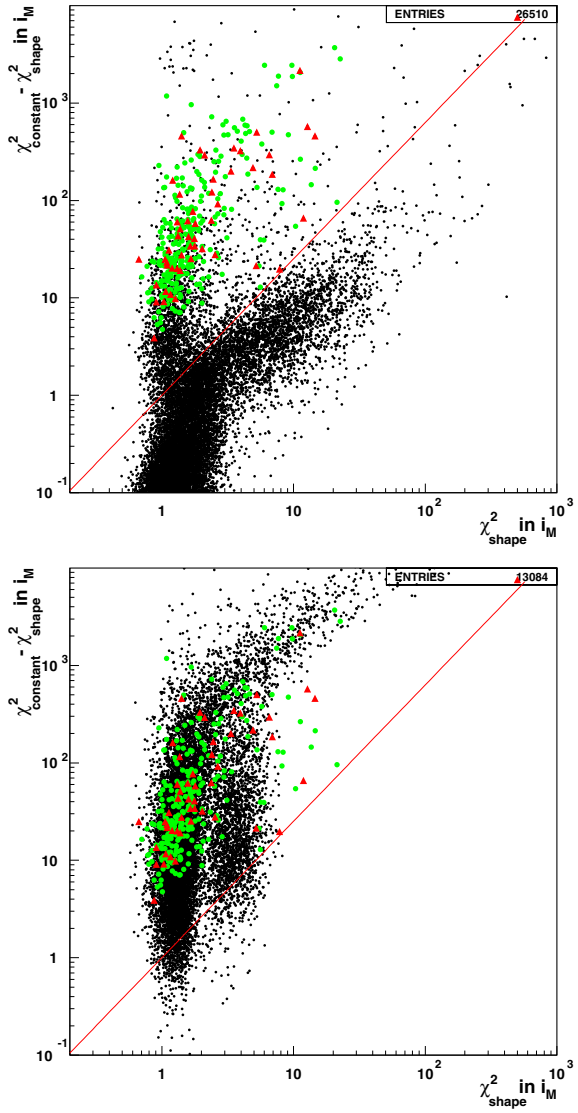


**Fig. 3.** Difference in reduced $\chi^2$ between $i_M$ light curve fits by a constant and by an SN-like shape (see text), as a function of the latter $\chi^2$. All cuts of the SN selection previous to that illustrated in this figure have been applied. Black dots stand for SNLS data (*top*) and synthetic SN Ia events (*bottom*). In both plots, green squares (resp. red triangles) are data events identified by spectroscopy as Type Ia (resp. core-collapse) SNe. Events above the curve are selected by the analysis.

the events selected by all previous cuts are compared with simulated SNe Ia (this comparison is further discussed in Sect. 3.3.2). Also highlighted in the plots are the spectroscopically identified events contained in our sample. A clear separation is observed between SN events and the bulk of the detections. After this cut, the number of events was reduced by a factor ∼10. While this cut is more discriminating than that on the off-variation $\chi^2$, they proved to be complementary, as part (∼12%) of the events rejected by the first cut would pass the second one.

#### 3.1.3. Star rejection

Events at this point were still contaminated by stars, either truly variable stars or bright stars leading to saturated signals at some epochs. We discarded detections within 3 $\Delta_{PSF}$ from stars in the catalogue described in Sect. 2.4, where $\Delta_{PSF}$ is the half-width of the PSF in the $i_M$ reference images. Saturated signals from bright stars lead to light curves with large flux changes over a few epochs. Events whose $i_M$ flux varied by more than 70% between the date of maximum flux and the two closest epochs in the same season were thus rejected. The above two cuts reduced the number of remaining detections by 12%. If they were applied instead of the constraint on the off-variation $\chi^2$, the reduction factor at that level would be similar (46% instead of 49%) but the sample remaining after the selection on the difference in reduced $\chi^2$ would increase by 65%. The three cuts previously described are thus necessary to achieve a significant rejection against background.

**Table 2.** Effect of the SN selection cuts.

| Cut | Events | Ia | CC | $\epsilon$(Ia) |
|---|---|---|---|---|
| Detection in $i_M$ | 295 683 | 278 | 55 | 0.96 |
| Variations in $i_M$ and $r_M$ | 193 104 | 277 | 55 | 0.94 |
| Consistent $t_{max}$ in $i_M$ and $r_M$ | 52 284 | 276 | 53 | 0.93 |
| Cut in $\chi^2_{off}$ | 26 510 | 276 | 52 | 0.93 |
| $\chi^2_{constant} - \chi^2_{shape}$ cut in $i_M$ | 2474 | 276 | 52 | 0.93 |
| Star veto | 2165 | 275 | 52 | 0.92 |
| Sampling cuts in $i_M, r_M$ | 1674 | 253 | 43 | 0.79 |
| Sampling cuts in $g_M, z_M$ | 1571 | 246 | 42 | 0.73 |
| Consistent $t^{fit}_{max}$ in $i_M$ and $r_M$ | 1483 | 246 | 42 | 0.73 |

**Notes.** The table details the effect of the cuts on the first three years of SNLS data: all detections (Col. 2), subsamples of events identified by spectroscopy as Type Ia and core-collapse SNe (Cols. 3 and 4). The last column indicates the efficiency of the cuts for bright SNe Ia, derived from synthetic SN Ia light curves at low magnitudes ($m_{0i} < 23$).

#### 3.1.4. Sampling requirements

Quality criteria ensuring sufficient temporal sampling of the light curves complete the selection. In the $i_M$ and $r_M$ bands, at least one pre-max epoch and one post-max epoch were required in an interval ranging from 30 days before the date of maximum flux in each filter up to 60 days after that date. These conditions were found appropriate for SN events, even fast-declining ones like SNe Ia which on average have time constants $\tau_{rise} \sim 4$ days and $\tau_{fall} \sim 20$ days in the $i_M$ and $r_M$ bands. In the $g_M$ and $z_M$ bands, at least two epochs were required in a similar interval around the date of maximum flux in the $i_M$ filter. Finally, the dates of maximum $t^{i_M}_{max}$ and $t^{r_M}_{max}$ from the fits by formula (1) were required to be within 50 days of each other, as more than 99% of both the synthetic SNe Ia and the spectroscopically identifed SN data events were observed to satisfy this condition.

#### 3.1.5. Results

At the end of the SN selection, a set of 1483 events is retained. The effect of the cuts on data is detailed in Table 2, which also gives the output of the cuts on spectroscopically identified supernovae and on simulated SN Ia light curves (as described in the next two sections).

### *3.2. Comparison with the SNLS real-time selection*

The SNLS real-time SN selection procedure is described in Perrett et al. (2010). It relies on real-time detection of variable events based on photometry, combined with a spectroscopic follow-up of the candidates which were both likely SNe Ia, as determined from an analysis of their real-time light curves (Sullivan et al. 2006a), and bright enough ones to allow

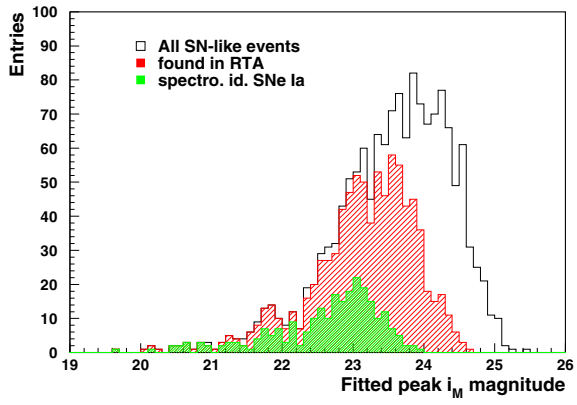


**Fig. 4.** Fitted $i_M$ peak magnitude distribution of selected SN-like events. Among these, events matched to SNLS real-time candidates (resp. spectroscopically identified SNe Ia) correspond to the red (resp. green) hatched histogram.

for conclusive spectroscopic measurements. Events fainter than $i_M^{AB} = 24.4$ or far beyond maximum light at detection time were not observed spectroscopically. Events with moderate brightness, $22.9 < i_M^{AB} < 24.4$ were qualified for spectroscopy if their fractional increase in brightness compared with their host galaxy was above a magnitude-dependent threshold (see Perrett et al. 2010, for more details). The spectroscopic observations were essential to confirm the nature of the real-time candidates and to obtain precise redshifts. As an example of how efficient the selection of targets for spectroscopy was, 71% of the first-year high redshift events sent for spectroscopy at the Gemini telescopes were confirmed to be Type Ia supernovae, either secure ("SN Ia") or probable Ia events ("SN Ia?"), as described in Howell et al. (2005).

In this section, we compare our photometrically identified SN-like events to those located by SNLS in real-time. The SNLS database[5] lists all variable events targeted by the real-time pipeline, as well as information returned by spectroscopy. Snapshots of these databases were extracted in January, 2009 and used to match the selected SN-like events of our photometric analysis with SNLS real-time candidates. Spectral data used for this matching (Howell et al. 2005; Bronder et al. 2008; Balland et al. 2009; and Walker et al. 2010) are identical to that used to define the SNLS 3-year sample for cosmological analyses (Guy et al. 2010; Conley et al. 2011).

Of the 1483 selected SN-like events, 865 (58%) could be associated with real-time candidates. Most of the remaining 618 events are faint events, with $i_M$ peak magnitudes above 23.4, as shown in Fig. 4. Besides background events, which are still present at this stage, these may also be interesting events too faint to be detected by the real-time pipeline. The matched events have the following types in the SNLS databases. 246 events are classified as SNe Ia and 42 are classified as core-collapse SNe, adding in both cases secure and probable events. These two subsamples are referred to as spectroscopically identified events throughout this paper. The other events are mainly classified as SNe (492 potential ones and 52 confirmed as supernovae by spectroscopy). A few AGN's (12 potential ones and 3 confirmed events) and possible stars (11 events, none confirmed) are also present. The type of these events is mostly based on real-time photometry, as most of them were not sent for spectroscopy. The break down of the SNLS database event types in the selected SN sample is presented in Table 3.

[5] https://legacy.astro.utoronto.ca

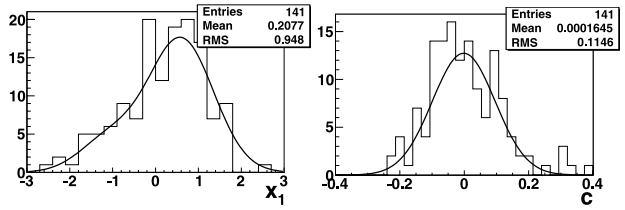


**Fig. 5.** $X_1$ and colour distributions of spectroscopically identified SNe Ia with redshift $z < 0.7$. The curves are used to produce synthetic light curves from the observed distributions.

Spectroscopically identified supernovae can be used to check the efficiency of the SN selection on bright supernova events. The SNLS database lists a total of 280 spectroscopically identified SNe Ia and 55 spectroscopically identified core-collapse events in the data covered by our photometric analysis. All of them are detected by our pipeline, except for two SNe Ia in D3, one outside our reference image and one from the presurvey phase. Of the 333 detected events, 288 passed the SN selection, as shown in Table 2. Most of the lost events were rejected by the sampling cuts. Those were not fulfilled due to either bad weather conditions or observations during the presurvey phase (42%), or truncation of the light curve at one end of the observation season (29%) or photometric points missing near maximum light because of CCD failures or full moon (24%).

### 3.3. SN selection efficiency for Type Ia supernovae

The efficiency of the SN selection was studied further with our set of synthetic SN Ia light curves. Those were simulated in the observed bands of MegaCam by the SALT2 package. Details about the simulation are given in the section below, comparison with data and selection efficiency are discussed in the next two sections.

#### 3.3.1. SN Ia light curve simulation

Synthetic SN Ia light curves were produced assuming a flat ΛCDM cosmology with $\Omega_M = 0.23$. Redshifts were simulated in the range from 0 to 1.2, with distances computed in the above cosmology. A volumetric distribution was assumed in order to reproduce the acceptance of the survey. The redshift dependence of the SN explosion rate is irrelevant for efficiency studies and was thus ignored at this stage. Values of the SALT2 $X_1$ and colour parameters were generated according to model distributions fitted to the 246 spectroscopically identified SNe Ia present in our selection (see Table 2), restricting to redshifts below 0.7 to avoid selection biases. A Gaussian distribution was used for the colour parameter, with mean and $\sigma$ values of 0. and 0.1 (see Fig. 5). For $X_1$, a double Gaussian was found more appropriate, with mean values of 0.06 and –1.07, $\sigma$ values of 0.8 and 0.7 and relative amplitudes equal to 0.25.

For each generated event, a rest-frame $B$-band peak magnitude, $m_B^*$, was computed as a function of the generated values of $X_1$, $C$ and of the luminosity distance at the generated redshift in the assumed cosmology, $d_L(z, \Omega_M)$ as:

$$m_B^* = M - \alpha X_1 + \beta C + 5\log_{10} d_L(z, \Omega_M)$$

using $M = -19.09$, $\alpha = 0.13$ and $\beta = 2.56$. A Gaussian spread with $\sigma = 0.14$ was applied to $m_B^*$ in order to allow for SN Ia intrinsic dispersion. The magnitude after dispersion was converted into a global normalisation factor $X_0$ according to the

**Table 3.** Event type break down at different analysis stages.

| Event | Analysis step | | |
|---|---|---|---|
| class | SN sel. | $+z_{gal}$ | Ia sel. |
| All events | 1483 | 1233 | 485 |
| In database | 865 | 739 | 388 |
| Ia Type | 246 | 208 | 175 |
| CC types | 42 | 38 | 1* |
| SN-like | 544 | 467 | 210 |
| AGN-like | 15 | 13 | 2 |
| Variable-like | 11 | 8 | 0 |
| Unknown type | 7 | 5 | 0 |

**Notes.** The break down is given in the photometrically selected SN-like events (Col. 2), in those events with a host galaxy photometric redshift (Col. 3) and in those finally kept as SN Ia events (Col. 4). The type of the event marked with an asterisk was revisited after this analysis (see Sect. 4.2).

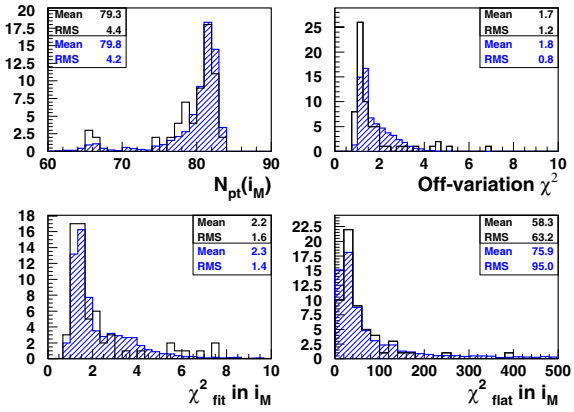


**Fig. 6.** Comparison between spectroscopically identified SN Ia data (open histogram) and synthetic light curves of bright SNe Ia (hatched histogram) in the D1 field. Distributions show the total number of points in the $i_M$ light curve and three $\chi^2$ variables used in the analysis (see text). The mean and rms of each distributions are indicated in the upper box for data and in the lower one for simulation.

relationship between $m_B^*$, $X_0$, $C$ and $X_1$ measured in the spectroscopically identified SNe Ia. Finally, dates of $B$-band maximum light were drawn uniformly in intervals starting 10 days before the beginning of the true observation periods and ending 5 days after their end. Each generated SN was also attributed a random position in one of the four fields of observations. Corrections for the Milky Way extinction of the SN Ia flux at the generated coordinates were applied in SALT2 using the dust maps of Schlegel et al. (1998) and the extinction law of Cardelli et al. (1989).

Detection and instrumental effects were then simulated in the following way. The detection efficiency model described in Sect. 2.2 was used to compute the detection probability of each synthetic event. Based on this probability, generated events were then randomly eliminated or kept for further processing. For each event passing this step, fluxes were computed at dates corresponding to true observations at the generated SN position in the mosaic. This allowed us to account for the observing strategy as well as for periods of lack of observations due to bad weather conditions or temporary CCD inefficiencies.

From these ideal fluxes, reconstructed fluxes and errors were then simulated according to reference distributions determined from the 278 spectroscopically identified SNe Ia that we detected (see Table 2). Distributions were those of flux errors and differences between the measured and the SALT2-estimated fluxes (thereafter called shifts in flux). Correlations between flux errors, flux values and flux shifts were taken into account when building the reference distributions. As around 20% of the light curves in the test-sample exhibit more points with a large shift in flux than expected from a pure random distribution, the reference shift distributions were determined separately for good and bad quality light curves. Observation dates showing systematic large shifts and errors were also described by reference distributions determined separately. A total of 20 000 synthetic light curves was generated.

#### 3.3.2. Comparison with data

Synthetic light curves are compared with spectroscopically identified SN Ia data in Fig. 6, where the first step of the selections described in Sect. 3.1 and an observed peak $i_M$-band magnitude below 23.5 were required. The agreement is reasonable. In particular, the simulation reproduces both the peak and the tail of the distributions of the various $\chi^2$ variables used in the selections.

The comparison is extended to all data in Fig. 3, showing the qualitative agreement between synthetic SN Ia light curves and identified SN data. In particular, there are two features that are reproduced by the simulation. The $\chi^2$ of the analytical fit, $\chi^2_{\rm fit}$, deteriorates at large $\chi^2$ differences, that is at low redshift, where formula (1) is less suited to fit SN light curves due to a secondary maximum in the near-infrared rest-frame light curves that SNLS observes in the $i_M$-band at low redshift. Second, at moderate $\Delta\chi^2$, the $\chi^2_{\rm fit}$ distribution has a tail at values above 2 which, in the simulation, is reproduced by bad quality light curves, i.e. light curves with a sizeable number of photometric points departing from the generated fluxes (see Sect. 3.3.1).

#### 3.3.3. Efficiency

The selection efficiency for Type Ia supernovae is presented in Fig. 7 as a function of the generated peak magnitude in $i_M$-band (full dots). The four fields were combined and, as fiducial cuts, we restricted all efficiency computations to those events whose generated date of $B$-band maximum light was strictly within the observing periods. For comparison, Fig. 7 gives also the efficiency for well sampled light curves (i.e. events passing the sampling cuts of the selection), showing that, at this stage of the analysis, the efficiency loss for bright events is due mostly to sampling requirements.

The efficiency for bright synthetic events is detailed in the last column of Table 2, which also gives that for spectroscopically identified SNe Ia in data. The efficiency from simulation ($0.73/0.96 = 76\%$) is lower than that for data events ($246/278 = 88\%$) since these have been submitted to tighter quality criteria to ensure conclusive spectroscopic measurements. As an example, bright events with a light curve starting past maximum light were not sent for spectroscopy, while they are included in the simulated sample. Restricting again the comparison to well sampled light curves in both simulation and data, the efficiencies become $246/246 = 100\%$ in data and $0.97/0.98 = 99\%$ in simulation, which gives confidence that reliable selection efficiencies are deduced from the simulation.

### *3.4. Redshift assignment*

The selected SN-like events were matched with galaxies in the catalogue described in Sect. 2.4. The match was considered

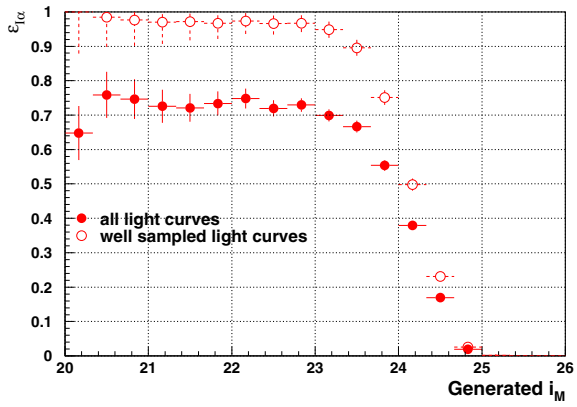


**Fig. 7.** Efficiency of the SN selection for Type Ia supernovae as a function of the peak magnitude in $i_M$-band, for all events (full dots) and for events with well sampled light curves (open dots). The efficiency was evaluated with synthetic SN Ia light curves.

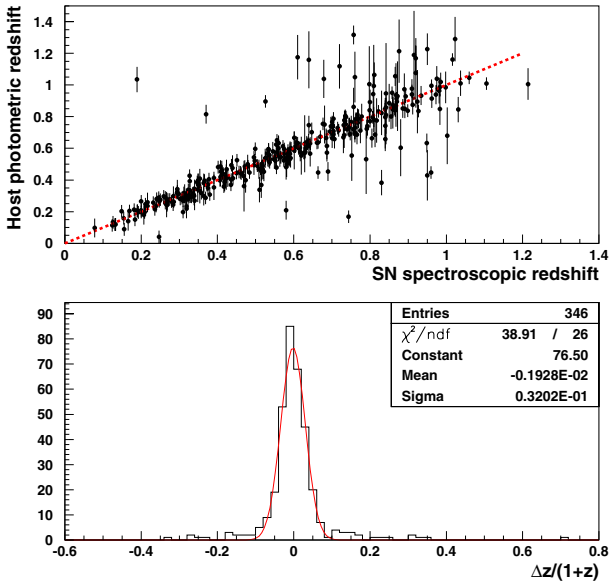


**Fig. 8.** Host galaxy photometric redshifts compared with event spectroscopic redshifts in the subsample of events with both measurements available at the end of the SN selection. The resolution of galaxy photometric redshift measurements is given in the bottom plot.

successful if the nearest galaxy from an event was found within a distance of $5r_{\rm gal}$, where the galaxy's effective radius, $r_{\rm gal}$, was defined as the half-width of the galaxy in the direction of the event and derived from the A, B and $\theta$ SExtractor parameters. In this procedure, galaxies so faint that no size measurement could be performed (typically fainter than $i_M \sim 24.5$) were assigned a size of 1 pixel and were considered only if no bright galaxy was found in the vicinity of the event. The choice of the $5r_{\rm gal}$ threshold was a compromise between host finding efficiency and accidental mismatching. Of the 1483 selected SN-like events, 1352 (91%) had matched hosts and 1233 of these (91%) had a photometric redshift which was then attributed to the event. The types of these events as found in the real-time database of SNLS (see Sect. 3.2) are listed in Table 3.

Host galaxy photometric redshifts were compared to event spectroscopic redshifts in the subsample of 346 selected SN-like events which have both measurements. The result is shown in Fig. 8. In most cases, the two redshift measurements agree and the galaxy photometric redshifts provide a resolution of $\sigma_{\Delta z/(1+z)} \sim 3\%$ in the central part of the distribution. However, 5.2% (resp. 10%) of the galaxy photometric redshifts depart from the spectroscopic redshifts by more than 5 (resp. 3) $\sigma$. Such differences can be explained by incorrect SN-to-galaxy associations or by bad galaxy photometric redshifts. The latter effect is likely to be the main reason for the deviations. According to Ilbert et al. (2006) 3.7% of the galaxy photometric measurements are to be expected with $\Delta z/(1+z) > 0.15$, for a sample of galaxies with magnitudes below 24 in $i_M^{AB}$, which corresponds to the range of host galaxy magnitudes in this study.

Incorrect redshift assignments are likely to generate significant systematic biases in the subsequent photometric SN Ia selection, especially at large ($z > 0.6$) redshifts, where most of the incorrect assignments occur (see Fig. 8). Special care was thus devoted to identify and reject most of these events in the SN Ia selection criteria that are described in the next section. As synthetic light curves provide an important tool to define the selections, host galaxy photometric redshifts were also simulated for the sample of synthetic light curves. Redshifts were generated according to a Gaussian distribution in $\Delta z/(1+z)^2$, to account for the fact that the reliability of the galaxy photometric redshifts decreases significantly for fainter objects (Ilbert et al. 2006). Redshift outliers were generated with a Gaussian distribution in $\Delta z/(1+z)$ and assuming their rate rises linearly with redshift. Parameters for this simulation were derived from the comparison between host galaxy photometric redshifts and event spectroscopic redshifts in the data, using the test-sample of 346 events already mentioned. Finally, the fraction of simulated events with a host redshift after the SN selection was given the same probability as observed in the data.

### 3.5. Summary

The total sample of 1233 SN-like events with a host galaxy photometric redshift is the starting point of the SN Ia search described in the next section. A measurement of the rate of core-collapse supernovae at low redshift was also deduced from that sample, as described in Bazin et al. (2009)[6].

## 4. SN Ia selection

The photometric SN Ia selection cuts were designed to discriminate SNe Ia from core-collapse supernovae (SNe CC) and to assess the reliability of the redshift assignment. The search was restricted to normal SNe Ia only, and relied on the SALT2 light curve fitter. As for the SN selection, the criteria were set up using spectroscopically identified supernovae present in our sample and synthetic SN Ia light curves as qualitative guidelines.

### 4.1. Selection criteria

The four-band light curves of each event were fit simultaneously with SALT2, fixing the redshift to the host galaxy photometric redshift, to derive the date of $B$-band maximum light $t^B_{\rm max}$, the colour $C$, the stretch-related parameter $X_1$ and the rest-frame $B$-band peak magnitude $m^*_B$ under the assumption that the event was a SN Ia. The fit converged for 98% of the events.

[6] This paper used a preliminary flux calibration resulting in slight differences in the analysis (e.g. 1207 SN-like events with a host galaxy photometric redshift instead of 1233).

#### 4.1.1. Light curve sampling

To ensure that meaningful SALT2 parameters were obtained, tighter quality cuts were applied w.r.t. the SN selection. Defining the event rest-frame phase as $\tau = (t_{\rm obs} - t^B_{\rm max})/(1 + z_{\rm gal})$, events were required to fulfil the following minimum conditions[7]:

(i) at least one measurement in the range $-10 < \tau < +5$ days for a reasonable estimate of $t_{\rm max}$ and thus of the peak magnitude;
(ii) at least one measurement in the range $+5 < \tau < +20$ days for a reasonable shape evaluation;
(iii) at least one colour among $(g-i)$, $(r-z)$ and $(i-z)$ with at least one measurement in each band in the range $-10 < \tau < +35$ for a reasonable Ia/CC discrimination (see Sect. 4.1.4).

After these cuts, the selected sample contained 1152 events, among which 203 (resp. 35) were confirmed as SNe Ia (resp. SNe CC) by spectroscopy. The remaining selections intended to enrich the sample in actual SN Ia events with correct assigned host galaxy photometric redshifts.

#### 4.1.2. $\chi^2$ requirements

To reject SN Ia light curves with a poor fit and to start eliminating non-Ia SNe, cuts were applied to the $\chi^2$ per degree of freedom in each filter, $\chi^2 < 10$ in the $g$ filter and $\chi^2 < 8$ in the $r, i, z$ filters. In addition, the $\chi^2$ per degree of freedom of the overall fit was required to be less than 6. Seven spectroscopically confirmed SNe Ia were rejected by these conditions. Two were assigned an incorrect host photometric redshift, the other five exhibited noisy light curves. These cuts also discarded nine spectroscopically confirmed SNe CC, all of the SN II type.

The light curve fit with SALT2 only included MegaCam filters corresponding to the redshifted wavelength interval between 290 nm and 700 nm, where the SN Ia model is defined with sufficient accuracy (see Guy et al. 2007 for details). Filter $g_M$ was thus only used below a redshift of about 0.68, while $z_M$ was considered only for a redshift larger than 0.26. Outside these redshift intervals, SNe Ia are expected to give no significant signal in these bands, but other types of supernovae may have a different behaviour. Comparing the observed flux in the unfitted bands to that corresponding to the SALT2 fit can give a complementary constraint against core-collapse events, as well as against incorrect redshift assignments in true SNe Ia.

The $\chi^2$ per degree of freedom with respect to the SALT2 best fit was thus computed in the unfitted bands and required to be less than 6 in $g_M$, and less than 3 in $z_M$. This criterion is stronger than that for the bands entering the fit, to compensate for the fact that the subsequent selections are looser for events which do not have all bands included in the fits. Ten spectroscopically confirmed SN Ia were eliminated by this second set of cuts. They were all assigned a bad host photometric redshift, with $\langle |z_{\rm gal} - z_{\rm spe}| \rangle = 0.35$ compared to an average of 0.06 for the other confirmed SNe Ia. These cuts also rejected four spectroscopically confirmed core-collapse events (two SNe II, two SNe Ib/c) because of their high $\chi^2$ in $z_M$.

[7] These requirements are very similar to those used to define the SNLS 3-year cosmological samples (Guy et al. 2010).

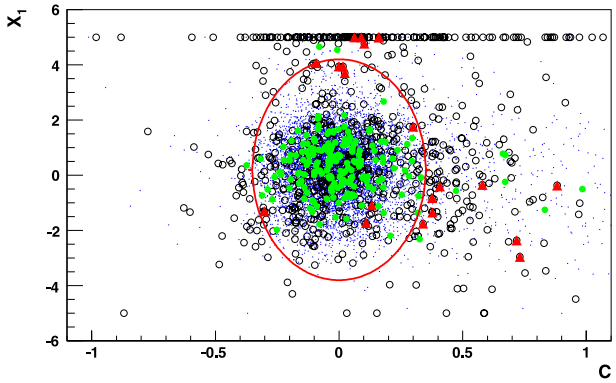


**Fig. 9.** $X_1$ vs. $C$ for synthetic SNe Ia (blue dots) and for data (all other symbols), after sampling and $\chi^2$ constraints have been applied. Green filled circles and red triangles stand for spectroscopically identified SNe Ia and SNe CC present in our sample, respectively. Open black circles stand for data events with no spectroscopic identification. Events outside the red ellipse are rejected. The pileup at $X_1 = 5$ is due to an upper bound encoded in the fitter.

#### 4.1.3. Stretch and colour constraints

As a further discrimination between SN Ia and non SN Ia events, a constraint was applied on the fitted $X_1$ and colour parameters, requiring

$$\left(\frac{X_1 - 0.2}{4.0}\right)^2 + \left(\frac{C}{0.35}\right)^2 < 1$$

as illustrated in Fig. 9. The constraint accounts for the offset of 0.2 observed in the stretch distribution, as shown in Fig. 5. Such an offset may reflect the higher number of high stretch SNe Ia observed at high redshift due to the increased fraction of star forming host galaxies in the past universe, which lead to more luminous supernovae (Howell et al. 2006; Sullivan et al. 2010).

While the lower bound on $X_1$ only removed a few relatively short and faint (average peak magnitude in $i_M$ of 25) data events, the upper bound discarded a large number of long duration events among which seven spectroscopically confirmed SNe CC, all of SN II type. On the other hand, the constraint on $X_1$ removed a negligible fraction (1%) of the synthetic SNe Ia.

The constraint on the fitted colour relies primarily on the observation that, while SN Ia colours were centred around 0 (with a rms of 0.11), the spectroscopically identified core-collapse events in our sample exhibited an average colour $\langle C \rangle = 0.3$. Requiring $C < 0.35$ rejected nine of these, mostly SN Ib and SN Ic events.

The cut on colour also allowed the rejection of SNe Ia where the associated host galaxy photometric redshift, $z_{\rm gal}$, was far from the true one. As an illustration, Fig. 10 presents the difference between $z_{\rm gal}$ and the more precise spectroscopic redshift, $z_{\rm spe}$ as a function of the fitted event colour, for events with both redshift assignments. Extreme colours in identified SNe Ia are mostly associated with inaccurate galaxy photometric redshift measurements. Synthetic SNe Ia show the same trend. The accuracy with which the colour of a true SN Ia is recovered, is indeed directly related to the reliability of the redshift assignment. As an example, about 70% of the synthetic light curves with $\left|z_{\rm gal} - z_{\rm spe}\right| > 0.2$ have $|C|$ above 0.35.

#### 4.1.4. SALT2 colour–magnitude diagrams

The last criteria to reject non SN Ia events were based on colour-magnitude diagrams from SALT2 fitted magnitudes. In these

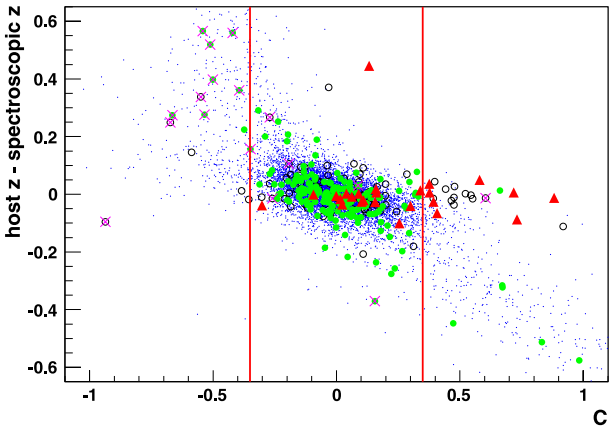


**Fig. 10.** Difference between redshift assignments as a function of SALT2 fitted colour. Same colour code and level of selections as in Fig. 9, except for pink crosses which indicate data events rejected by the $\chi^2$ selections in unfitted bands. Red lines indicate the extreme values of the colour cuts.

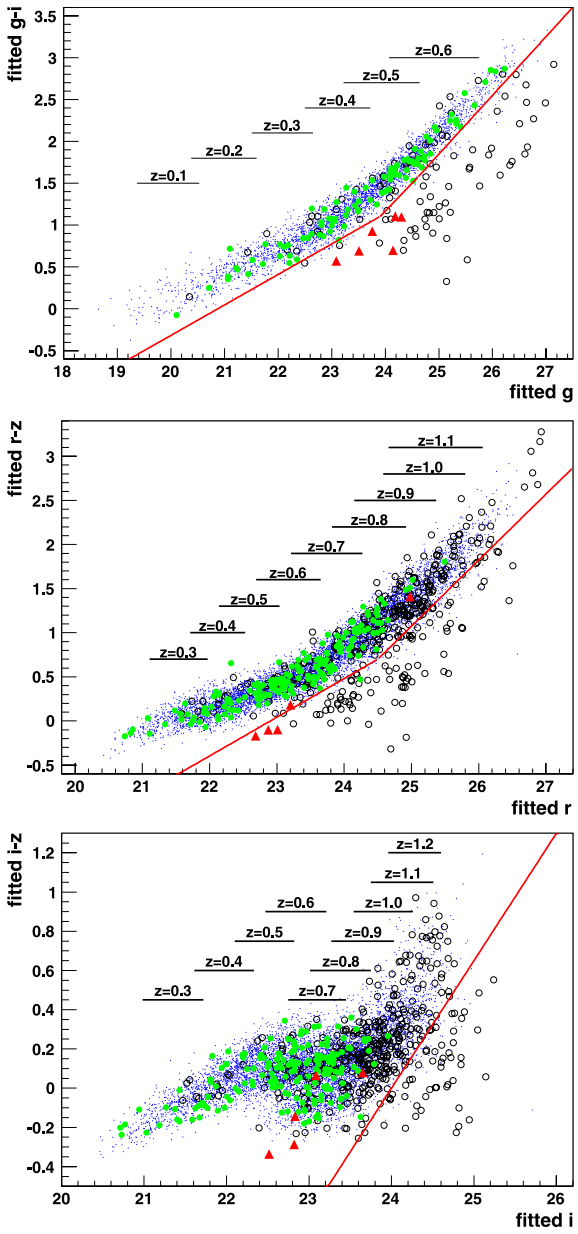


**Fig. 11.** Colour–magnitude diagrams based on SALT2 fitted magnitudes for events that passed all previous constraints up to $X_1$ and $C$ cuts. Same colour code as in Fig. 9. Events below the lines were rejected. $1\sigma$ magnitude ranges are indicated for 0.1 redshift bins centred on the indicated redshift values (vertical locations of the segments are arbitrary).

diagrams, Type Ia supernovae populate a thin band while core-collapse supernovae lie in a broad region which is shifted w.r.t. the SN Ia band. To emphasize the colour and magnitude difference between the two classes of events, the following diagrams were chosen: $g - i$ vs. $g$, $r - z$ vs. $r$ and $i - z$ vs. $z$ (Fig. 11, top to bottom), where $g$, $r$, $i$ and $z$ are the magnitudes in the MegaCam filters computed from the SALT2 best fit model, at the date of $B$-band maximum light. Note that events entered these diagrams only when the filters of interest were actually considered in the fit (see Sect. 4.1.2). The first diagram was thus used for low redshift events, $0.16 < z < 0.68$, the second one was considered in the redshift range $0.26 < z < 1.15$, while the third one applied for $0.26 < z$. Events at the highest redshift ($z > 1.15$) were thus tested only through the third diagram.

The $g - i$ vs. $g$ diagram proved to be very helpful in reducing the remaining background from core-collapse supernovae, as most of those we could detect were at low redshift, and, in this diagram, appeared fainter than actual SNe Ia for the same $g - i$ colour. Although the magnitude dispersion of the SNe CC is close to 1 mag, this diagram offered a good discrimination between CC and Type Ia supernovae. Part of the SNe CC were detected at high enough redshift to enter the $r - z$ vs. $r$ or $i - z$ vs. $i$ diagrams. A similar trend was observed there, with a population distinct from the SNe Ia, lying at fainter magnitudes for a given colour. The separation between the two populations in these diagrams is however less pronounced than in the $g - i$ vs. $g$ diagram.

Altogether, the three diagrams were useful to complete the reduction of the CC supernova background. Note however that the spectroscopically confirmed SNe CC that would be rejected by the colour-magnitude diagrams alone, i.e. not considering any of the previous SN Ia selection criteria, are all typed as either SN-II or SN-IIP. In the colour-magnitude diagrams, the SNe Ib/c often lay close to the upper limit of the SN Ia band and could not be identified unambiguously.

### 4.1.5. Results

At the end of the selection, 485 SN Ia candidates were selected. The overall selection efficiency is given in Fig. 12 as a function of the peak magnitude in the $i_M$ filter, for all synthetic events (full squares) and for events with well sampled light curves (open squares) defined as in Sect. 3.3.3. For the latter, the bright event efficiency is 67%. It would be 80% if all events were assigned a host galaxy photometric redshift. This number represents the intrinsic performance of our selection for bright SNe Ia, regardless of the survey observing strategy or the availability of host redshifts.

The effect of the different selection criteria is detailed in Table 4, where the selection efficiency is given for bright events with well sampled light curves. As for the SN selection, the efficiency of the SN Ia selection criteria from simulation ($0.67/0.97 = 69\%$) agrees well with that for spectroscopically identified SNe Ia ($175/246 = 71 \pm 3\%$).

### 4.1.6. Discussion

The use of colour-magnitude diagrams in the selection may generate biases in the selection as a function of redshift. To check

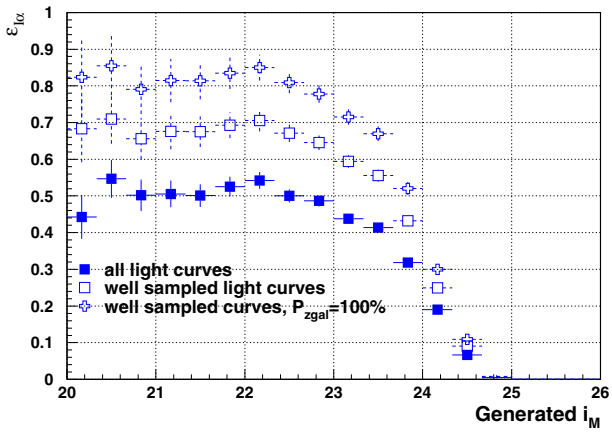


**Fig. 12.** Efficiency of the SN Ia selection for Type Ia supernovae as a function of the peak magnitude in $i_M$-band, for all events (full squares) and for events with well sampled light curves, when the host galaxy redshift assignment probability is included (open squares) or not (crosses). The efficiency was evaluated with synthetic SN Ia light curves.

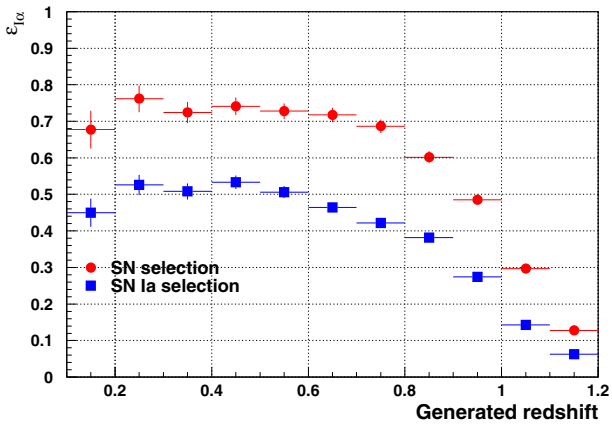


**Fig. 13.** Selection efficiency from synthetic SN Ia light curves as a function of the generated redshift, at different stages of the analysis.

**Table 4.** Effect of the SN Ia selection cuts.

| Cut | Events | Ia | CC | $\epsilon$(Ia) |
|---|---|---|---|---|
| SN selection | 1483 | 246 | 42 | 0.97 |
| Host redshift available | 1233 | 208 | 38 | 0.80 |
| Light curve sampling | 1152 | 203 | 35 | 0.75 |
| $\chi^2$ | 951 | 186 | 22 | 0.68 |
| $X_1$ and colour | 596 | 176 | 7 | 0.67 |
| $g-i$ vs. $g$ | 539 | 176 | 1* | 0.67 |
| $r-z$ vs. $r$ | 490 | 175 | 1* | 0.67 |
| $i-z$ vs. $z$ | 485 | 175 | 1* | 0.67 |

**Notes.** The effect of the cuts is given for all detections (Col. 2), for the subsamples of events identified by spectroscopy as Type Ia and core-collapse SNe (Cols. 3 and 4), and for synthetic bright SNe Ia ($m_{0i} < 23$) with well sampled light curves (Col. 5). The type of the event marked with an asterisk was revisited after this analysis (see Sect. 4.2).

this, we show in Fig. 13 the selection efficiency as a function of the generated redshift (see Appendix B for the colour and $X_1$ variations). The dependence seen in Fig. 13 follows mostly from the fact that the selection is easier for brighter SNe Ia, i.e. for lower-redshift, bluer and higher-stretch events. The SN Ia selection efficiency starts to decrease at redshifts above 0.6 while the SN selection efficiency plateau extended up to $z \sim 0.8$. We checked that this decrease is due to the cuts on colour and on the reduced $\chi^2$ from the unfitted bands, which are essential to reject

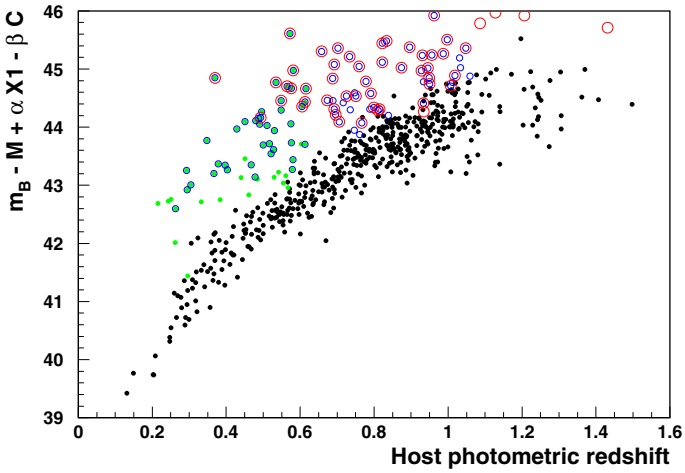


**Fig. 14.** Hubble diagram for data events at different levels of the photometric SN Ia selection. Black dots stand for events at the end of the selection, green filled (resp. open blue) circles for events rejected by the constraints on the SALT2 fitted $g-i$ vs. $g$ (resp. $i-z$ vs. $i$) colour-magnitude diagram, open red circles for events rejected by the constraints on the SALT2 fitted $r-z$ vs. $r$ diagram.

non-SNIa contaminants and true SNe Ia which were assigned an incorrect redshift.

The colour-magnitude diagrams used in the above analysis are based on SALT2 fitted magnitudes and not on colours and magnitudes derived directly from observations. We checked that using magnitudes at the SALT2 date of $B$-band maximum light derived from fits to the light curves with formula (1) would indeed lead to a poorer discrimination between SNe Ia and contaminants, due to larger dispersions, especially in the $r-z$ vs. $r$ and $i-z$ vs. $i$ diagrams. More quantitatively, applying the selections described in Sect. 4.1.4 on these diagrams would lead to 6% less efficiency and 75% more contamination by CC SNe (see Sect. 4.5).

The impact of the colour-magnitude constraints based on SALT2 fitted magnitudes is illustrated in Fig. 14 which shows the Hubble diagram of the sample of photometrically selected events (see Sect. 5 for more details about the distance modulus computation) as well as events rejected by each constraint. On average, the average distance modulus of the rejected events is 1.34 mag larger than that of the selected sample, with a rms of 0.61 mag, almost twice that of the selected sample. Keeping events whose distance modulus is within 0.55 mag above the Hubble flow would lead to similar SN Ia efficiency, core-collapse contamination and sample of data events as the colour-magnitude diagram constraints used in this analysis. The two methods are thus equivalent.

As mentioned in Sect. 3.4, redshift outliers were present in a significant fraction of the selected SN events, e.g. 10% of those had redshifts which were $3\sigma$ outliers. Figure 15 shows the comparison between spectroscopic and host galaxy photometric redshifts at the end of the SN Ia selection. Highlighted in the plot is the effect of the $\chi^2$ and colour requirements, which prove to be helpful to reject events which were assigned a redshift outlier. At the end of the SN Ia selection, 1.4% (resp. 5.5%) of the host galaxy photometric redshifts depart from the spectroscopic ones by more than 5 (resp. 3) $\sigma$. The outlier fractions at the SN selection level have been reduced by a factor 4 and 2, respectively. There is no change in the redshift resolution, but the redshift distribution is now much closer to a Gaussian, as shown in the bottom plot of Fig. 15.

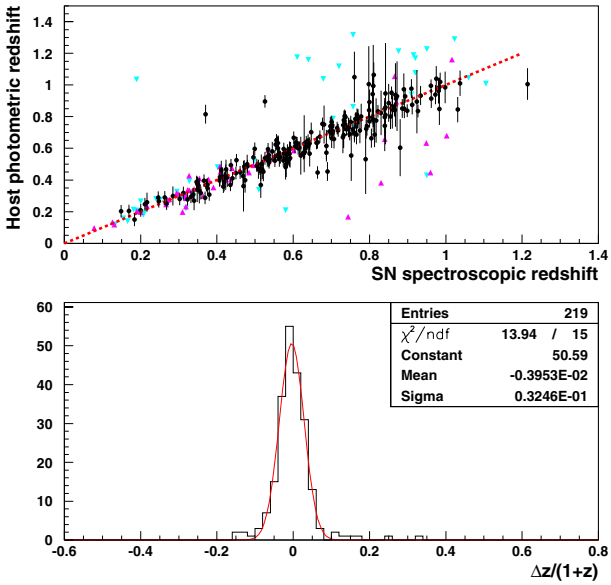


**Fig. 15.** Host galaxy photometric redshifts compared with event spectroscopic redshifts in the subsample of events with both measurements available after all SN Ia selection criteria have been applied (black dots). Downward light blue (resp. upward pink) triangles stand for SN-like events rejected by the $\chi^2$ (resp. colour) cuts of the SN Ia selection. The redshift resolution at the end of the SN Ia selection is given in the bottom plot.

Summarising, with the above photometric selection, well sampled light curves of bright SNe Ia are selected with an average efficiency of 67%, which includes the 83% efficiency of the host galaxy photometric redshift assignment. Photometric redshifts derived from supernova light curves would offer a better redshift assignment probability than what we achieved here. In Palanque-Delabrouille et al. (2010) we set up such a method based on SALT2 and tested it with the synthetic SN Ia light curves and the photometric data sample described in the previous sections. Combining both supernova selection and redshift determination from photometry will be the subject of another paper.

In the next sections, we pursue the discussion on the present analysis, comparing its output to that of the real-time SNLS analysis and evaluating the contamination of the selected sample by residual core-collapse supernovae.

### 4.2. Comparison with the SNLS real-time selection

As in Sect. 3.2, events of the photometric sample were associated with SNLS real-time candidates. The break-down of the event types is summarised in Table 3. Out of the 485 candidates, 388 (80%) were detected in real-time. Of these, 45% are spectroscopically identified SNe Ia (adding up secure and probable SNe Ia) and another 54% were typed (mostly photometrically) as SNe. The remaining 3 events have the following characteristics.

One event, SNLS 06D2bo was identified as having a spectroscopic redshift of $z = 0.370$, on the basis of strong [OII] and [OIII] emission lines from the host galaxy. The best match appeared to be the broad-lined SN 1998bw, so the event was classified as a possible CC SN. The event is highlighted in Fig. 11 (middle plot) as the red triangle at $r_M \sim 25$. It lands within the locus of points defined by SNe Ia. The photometric redshift of the host was much higher, $z = 0.82$, and agreed with the estimate of the redshift derived from fitting the SN light curve (using e.g. Sullivan et al. 2006a or Palanque-Delabrouille et al. 2010). The large discrepancy between the photometric redshifts (SN and host) and the spectroscopic one prompted us to re-examine the spectroscopic data. We soon discovered that the spectrum of an unrelated object had been extracted instead of SNLS 06D2bo. The data were reprocessed. SNLS 06D2bo is clearly a SN Ia, with a best fit redshift of $z = 0.79$. We have chosen to let the error in the extraction stand. It vindicates the accuracy of the technique we have developed to photometrically identify SNe Ia, and it indicates the level of human error in the analysis of the SNLS spectroscopic data.The impact of excluding this SN from this paper specifically and from the 3-year SNLS analyses more generally is negligible.

The other two candidates were considered as "AGN?" from their real-time light curves and were not sent for spectroscopy. The distances to their host galaxies are 0.2 and 0.3 $r_{\rm gal}$ where $r_{\rm gal}$ is the effective galaxy radius introduced in Sect. 3.4. These values are in the bulk of the distance distribution, which peaks near 0.01 $r_{\rm gal}$. There is no hint that these two events are highly centred, as would be expected for AGN's. Their light curves do not exhibit any peculiarity either when compared to normal SNe Ia. In both cases, the redshift of the associated host is in agreement with a supernova photometric redshift derived from the light-curves.

Finally, SNLS detected eight supernovae which were classified as peculiar Type Ia after spectroscopy, as described in Balland et al. (2009), Bronder et al. (2008) and Ellis et al. (2008): SNLS 03D3bb, SNLS 03D4cj, SNLS 03D4ag, SNLS 03D1cm, SNLS 04D3mk, SNLS 05D1by, SNLS 05D1hk, SNLS 05D3gy. Supernova SNLS 03D3bb is a super-Chandrasekhar Type Ia (Howell et al. 2006) with maximum light in the presurvey and does not pass the SN selection cuts. Supernova SNLS 03D1cm is a 1991T-like object, with $X_1 = 4.54$ and is therefore excluded by our cuts. Supernova SNLS 05D1by is rejected because of its red colour ($C = 0.66$). The other five events do not exhibit any sign of peculiarity in their light curves and are in our photometric sample.

### 4.3. Comparison with the SNLS 3-year cosmological sample

In Guy et al. (2010), SNLS describes a set of well sampled light curves for 252 Type Ia supernovae that was used to derive the 3-year cosmological analyses of the collaboration (Conley et al. 2011). The photometric SN Ia selection described in this paper recovers 172 events of that sample. The lost fraction (32%) breaks down into 6% due to SN selections, 16% due to host galaxy redshift availability and 10% due to SN Ia selections. Note that this result agrees with the efficiencies from synthetic SN Ia light curves that we quoted in Sect. 4.1.6.

### 4.4. Comparison with the SNLS sub-luminous SN Ia sample

González-Gaitán et al. (2011) provides a photometrically selected sample of 18 sub-luminous SNe Ia from SNLS data with $z < 0.6$. All but two of these SNe are included in the sample analysed in this paper. Among those 16 events, 7 were kept by our photometric selection and 9 were rejected because of insufficient temporal sampling (4), $\chi^2$ cuts (2) or extreme values of SALT2 colour or $X_1$ parameters (3). Despite the use of a light curve fitter trained on normal SNe Ia only, our photometric selection appears to have some efficiency on sub-luminous SNe Ia as well.

### 4.5. Contamination by core-collapse supernovae

Our set of 485 photometric SNe Ia candidates includes 175 spectroscopically identified SNe Ia (see Table 4). One other event was spectroscopically identified as a possible core-collapse supernova initially, but was later found to be a SN Ia after it was discovered that the wrong spectrum had been extracted. The remaining 309 events have no conclusive spectroscopic typing either because no spectra were obtained or because of insufficient spectral signal-to-noise. In this section we will estimate how many of the 485 events are, in fact CC SNe that were incorrectly identified photometrically as SNe Ia. Core-collapse supernovae are typically more than a magnitude fainter than SNe Ia so a CC SN is unlikely to be confused with a SN Ia unless its redshift is significantly overestimated so that its faintness is explained by its distance.

It is relatively simple to place an upper limit on the contamination at low-redshift, $z < 0.4$. Supernovae at these redshifts are spectroscopically unambiguous because of the visibility of the 615 nm Si II absorption feature characteristic of SNe Ia. While spectra for all SNLS CC SNe were not obtained, those that appeared to be possible SNe Ia during the early phase of the explosion were given high priority for spectroscopy. We can therefore expect that for $z < 0.4$ we have a complete spectroscopic sample of those CC SNe most likely to be photometrically selected as SNe Ia. Our photometric sample at $z < 0.4$ contains 35 spectroscopically identified SNe Ia and no spectroscopically identified CC SN, which gives a 95% CL upper bound of 3 core-collapse supernovae. The contamination of our sample at low redshift is thus expected to be less than ~3/35 ~9% at the 95% CL. This assumes that spectroscopic efficiencies at these redshifts are similar for Type Ia supernovae and for those among the CC events that would appear as possible SNe Ia.

To refine this estimate and extend it to higher redshifts, we build a light curve model for CC SNe based on the SNLS sample of low-redshift ($z < 0.4$) supernovae, using the analytical model of Eq. (1) to describe the light curves. To set up the simulation, we defined, as a CC test-sample, the set of 117 low redshift events used in Bazin et al. (2009) to measure the CC rate at $z < 0.4$. The 117 events include the 33 spectroscopically identified CC SNe and 84 events with no spectra and not photometrically selected as SNe Ia. To these, we added 9 spectroscopically identified CC SNe that had either no host galaxy photometric redshift or a host galaxy photometric redshift above 0.4.

As detailed in Sect. 3, the analytical model of Eq. (1) describes the signal with four parameters in each filter, namely an amplitude, a date of maximum, a fall time and a rise time. Distributions of these parameters in the $i_M$ filter, as well as correlations between these and the parameters in each of the other filters were measured in the test-sample and parametrised for their subsequent use in the light curve simulation. This was done separately for events with plateau light curves (35 events, either events spectroscopically confirmed as SNIIP or events with fall times above 60 days) and for fast-declining events (77 events, either events spectroscopically identified as SN Ib, SN Ic or SN II or events with fall times below 40 days). No further distinction could be made in the latter category between Type Ib/c and Type II supernova light curves.

The test-sample is mostly limited at low redshift, below $z \sim 0.4$. In order to model the average redshift dependence of the amplitudes, the parameters of the low-redshift supernovae were redshifted to mimic supernovae at higher redshifts. The amplitudes in the $r_M$ and $g_M$ bands at a low redshift $z$ were thus

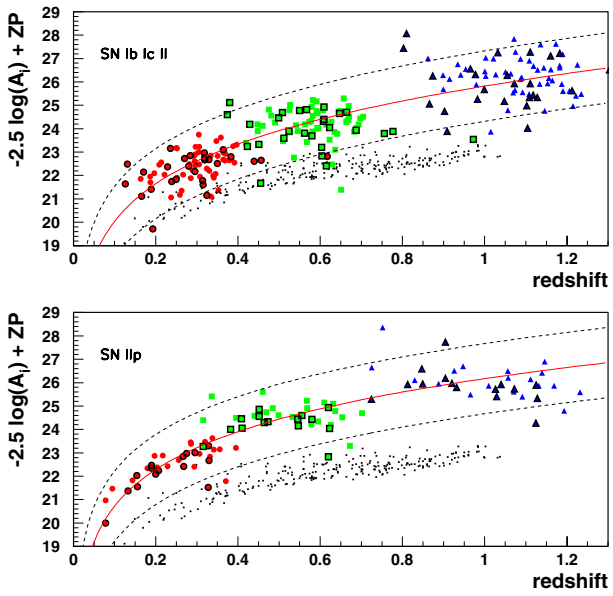


**Fig. 16.** Magnitude corresponding to $A_i$, the $i_M$-band amplitude parameter of the model representing SN light curves, as a function of redshift, for fast-declining CC supernovae (*top*) and plateau ones (*bottom*), as measured in the 3-year SNLS data. Red dots come from fits to $i_M$-band light curves, green squares (resp. blue triangles) from fits in the $r_M$ (resp. $g_M$) filter taken as estimates of $A_i$ at higher redshifts (see text). Symbols with black borders indicate spectroscopically identified events. The curves are fits to the average redshift dependence of the magnitude, excluding points outside the dashed lines. As a comparison, black dots give magnitudes from spectroscopically identified SNe Ia.

taken as estimates of $A_i$ at a higher redshift $z_i$ defined as:

$$1 + z_i \equiv \frac{\lambda_i}{\lambda}(1 + z)$$

after rescaling by:

$$A_i \equiv A \frac{\lambda_i}{\lambda} \frac{d_L(z)^2}{d_L(z_i)^2}$$

where $\lambda_i$ and $\lambda$ are the mean wavelengths of the $i_M$ and $r_M$ or $g_M$ filters and $d_L(z)$ is the luminosity distance for the cosmology introduced in Sect. 3.3.1. In the above formulas, $z$ was taken as the spectroscopic redshift whenever available (50% of the cases), and as the host galaxy photometric redshift otherwise. Amplitudes in the $r_M$ and $g_M$ filters were thus used to estimate the $i_M$ band amplitude $A_i$ at redshifts $0.4 < z_i < 0.7$ and $0.7 < z_i < 1.2$, respectively. Figure 16 presents the estimated $A_i$ as a function of $z_i$.

The average redshift dependence of the modelled $i_M$-band magnitude was fitted with the logarithm of a third order polynomial in the redshift $z_i$. The test-sample of plateau (resp. other CC) supernovae has a scatter of 0.5 mag (resp. 0.8 mag) around this average behaviour. Given the above scatters in magnitude, the dependence of our $A_i$ modelling with the reference cosmology assumed in the luminosity distance computation was found to be negligible. The fitted redshift dependence of the modelled $i_M$-band magnitude and the spread of the residuals around the latter were used to simulate $i_M$-band amplitudes according to a Gaussian distribution. Amplitudes in the other bands were simulated to reproduce the observed colours in the test-sample. The colours simulated at high redshift were checked to be identical to those for lower redshift supernovae in the appropriate (bluer) bands.

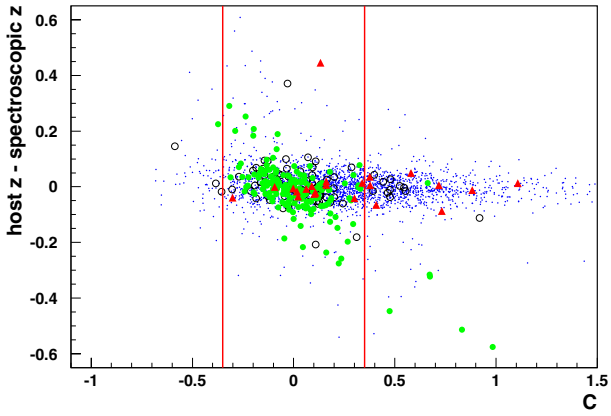


**Fig. 17.** Difference between redshift assignments as a function of the SALT2 fitted colour, for synthetic core-collapse events (blue dots) and data events (all other symbols), after all selections previous to that on SALT2 $X_1$ and colour (see text). Green circles (resp. red triangles) are data events present in our sample which have been identified as Type Ia (resp. core-collapse) supernovae by spectroscopy. Open black circles stand for data events with no spectroscopic identification.

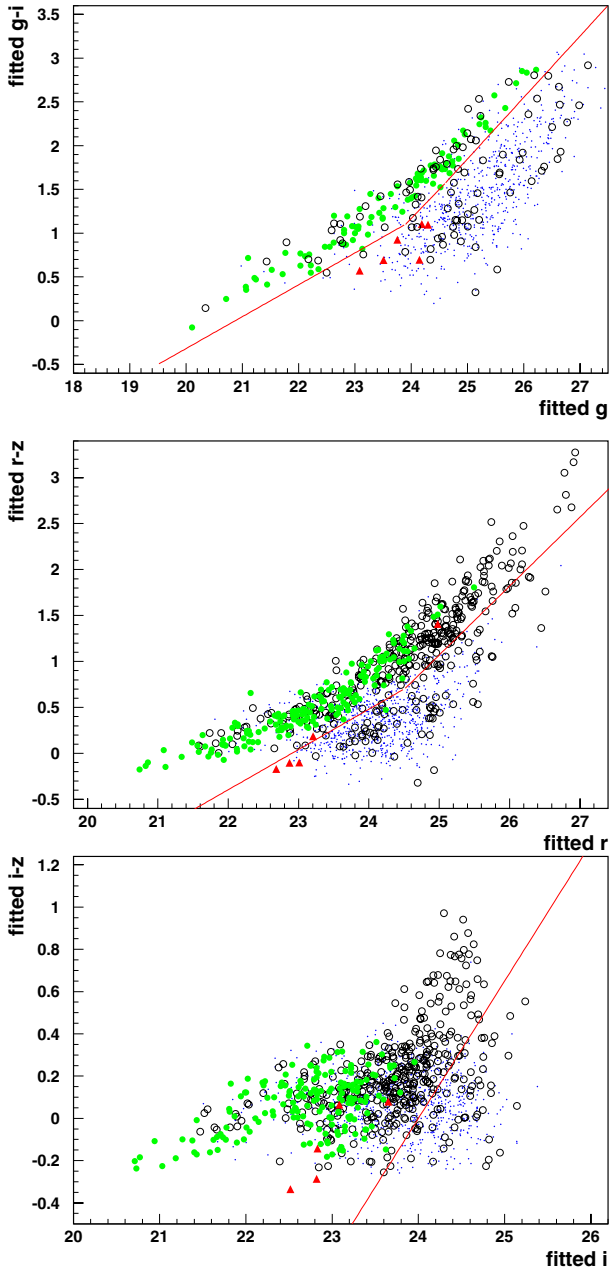


**Fig. 18.** Colour−magnitude diagrams from SALT2 fitted magnitudes used in the photometric SN Ia selection, for synthetic core-collapse events and data events that have passed all selections prior to those based on these diagrams. Same colour code as in Fig. 17.

We generated synthetic core-collapse light curves in the redshift range $0 < z < 1.2$. As in the SN Ia simulation, host galaxy photometric redshifts were also generated, in order to reproduce the selections of the analysis. A total of 40 000 light curves was simulated (20 000 in each category), of which 13% remained at the end of the SN selection. To illustrate the output of the simulation, Figs. 17 and 18 show some of the constraints used in the SN Ia selection, with SNLS data now compared with synthetic CC light curves. We observe that our simulation based on low-redshift events reproduces the distribution of spectroscopically identified CC SNe and of supernovae with no spectra.

The contamination of the photometric sample of SN Ia candidates by CC SNe was then derived as follows. Our synthetic light curve simulation assumed redshift-independent volumetric supernova distributions. To account for this, synthetic events were first weighted by the actual redshift dependence expected for the volumetric explosion rates, assuming the SN Ia rate to be proportional to $(1+z)^2$ (Pritchet et al. 1999) and the core-collapse SN rates to vary as the star formation rate, i.e. as $(1+z)^{3.6}$ (Hopkins & Beacom 2006). The numbers of weighted events passing the photometric SN Ia selections were then computed for the three samples of synthetic light curves (one for SNe Ia, one for SNe IIP and one for all other core-collapse SNe) in the redshift range $z < 1.2$. To normalise the SN CC and Ia simulations with each other, we used the CC to Ia volumetric rate ratio published in Bazin et al. (2009), that holds for low redshift ($z < 0.4$) events, in an absolute magnitude interval extending to 4.5 mag fainter than normal SNe Ia. The normalisation was set in order that weighted synthetic events reproduce the published ratio in the same conditions of redshift and magnitude.

After normalisation, we obtained a contamination of $17.6 \pm 3.9(stat.)$ supernovae in our photometric sample of 485 SN Ia candidates. Essentially all (99%) of the contaminating events are non-plateau core-collapse supernovae. The statistical uncertainty is mostly due to the small number of events in the sample of low-redshift CC SNe which led to the measurement of the CC to Ia volumetric rate ratio used in the above normalisation. The statistical uncertainty on that measurement was 20%.

Note that the synthetic CC events remaining at the end of the selections are at moderate host galaxy photometric redshift, $z_{\rm gal} \sim 0.5$ on average with an rms of 0.2 (see also Table 5) and, when reconstructed as SNe Ia by SALT2, exhibit positive colours (with a mean value of 0.15 and an rms of the same order) and a broad distribution of $X_1$ values (with a mean of –0.3 and an rms of 1.7). Moreover, the rate of $5\sigma$ outliers in host galaxy photometric redshift is 5% in this sample, slightly higher than the 1.4% observed in the whole photometric sample.

## 5. Comparison of event subsamples with and without spectroscopic identification

The sample of 485 SN Ia photometric candidates contains 175 spectroscopically identified SNe Ia, called hereafter the "identified sample", and 310 events with no spectral

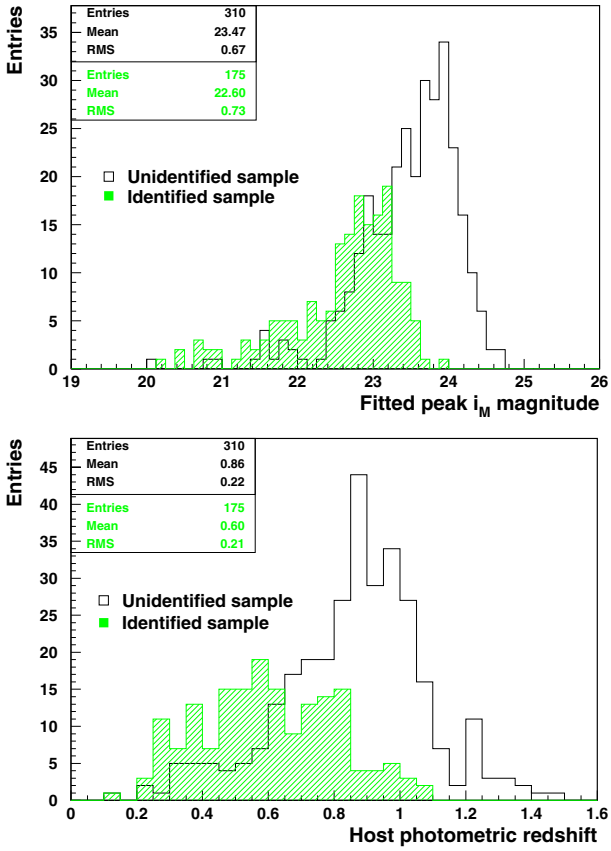


**Fig. 19.** Distributions of the SALT2 fitted $i_M$ peak magnitude (*top*) and of the host galaxy photometric redshift (*bottom*) for the identified (in green) and unidentified (in black) subsamples of photometrically selected SNe Ia.

**Table 5.** Contamination from core-collapse supernovae.

| Redshift | Events | CC |
|---|---|---|
| $z_{\rm gal} < 0.4$ | 49 | $4.4 \pm 1.1$ |
| $0.4 < z_{\rm gal} < 0.8$ | 196 | $11.1 \pm 2.5$ |
| $0.8 < z_{\rm gal}$ | 240 | $2.1 \pm 0.5$ |

**Notes.** The table shows the number of events passing the photometric SN Ia selection and the estimated CC contamination in three bins of host galaxy photometric redshift.

confirmation[8], called hereafter the "unidentified sample". The distribution of the peak magnitude in $i_M$ for the two subsamples is given in Fig. 19. The unidentified sample is about one magnitude deeper on average than the identified sample, as expected from the constraints to obtain a spectrum for the identified SNe Ia. This translates into an average redshift of 0.60 for the identified set and of 0.86 for the additional set.

### 5.1. Comparison of bright events

At bright magnitudes, $i_M < 23$, there are 110 identified events and 56 unidentified ones, all but 5 events found in the real time analysis. We traced back the reasons why these bright events missed a spectroscopic identification. A third of them had been detected in the real-time analysis, declared (from photometry) as probable SNe Ia and sent for spectroscopy. Insufficient quality of the spectrum, however, resulted in a spectroscopic redshift (usually from the host galaxy) but no typing of the supernova. Another third were also declared as probable SNe Ia but could not be scheduled for spectroscopic follow-up near maximum light. The last third were usually less convincing candidates according to their real-time, and thus partial, light curves.

[8] Note that event SNLS 06D2bo has been included in the unidentified sample.

**Table 6.** Comparison of events with and without spectroscopic identification.

| Parameter | Identified sample | Unidentified sample | KS proba |
|---|---|---|---|
| $C$ | $0.00 \pm 0.01$ | $0.02 \pm 0.02$ | 0.40 |
| $X_1$ | $0.23 \pm 0.08$ | $-0.01 \pm 0.13$ | 0.30 |

**Notes.** The mean values of SALT2 colour and $X_1$ are given for photometrically selected events with $i_M < 23$, split into subsamples with and without spectroscopic identification. Numbers in the last column are the Kolmogorov-Smirnov probabilities that the two distributions arise from the same parent distribution.

The characteristics of the two subsamples of bright events were compared, based on their complete light curves as reconstructed in this analysis. Their colour and $X_1$ distributions were found to be compatible, as summarised in Table 6. We also compared the colour-magnitude and $X_1$-magnitude relations in the two subsamples. For this purpose, the distance modulus of each event was defined from the SALT2 fitted $B$-band peak magnitude $m_B^*$, $X_1$ and colour $C$ as:

$$\mu_B = m_B^* - M + \alpha X_1 - \beta C \qquad (2)$$

using values of $M$, $\alpha$ and $\beta$ introduced in Sect. 3.3.1. Residuals were then computed from these distance moduli by subtracting $5 \log[P(z)]$ where $P(z)$ is a third-degree polynomial that we fitted on the total photometric sample in order to describe the mean redshift dependence of the distance modulus with no assumption on a specific cosmology model. The Hubble diagram residuals without the colour or $X_1$ term in the distance modulus are represented in Fig. 20. The figure shows the fit of the colour-magnitude and $X_1$-magnitude relations from the full sample of bright events, as fits from the two subsamples were found to be indistinguishable.

In conclusion, when restricted to the same range of $i_M$ peak magnitudes, the unidentified and identified samples of events do not exhibit significant differences.

### 5.2. Comparison of full samples

We now consider the full set of photometrically selected SNe Ia as an extension of the identified subsample towards fainter events, and estimate the impact on distance moduli of using the limited sample of spectroscopically identified SNe Ia. The Malmquist bias due to spectroscopic sample selections is an important issue in cosmology fits and was thoroughly studied in SNLS with Monte Carlo simulations. The results, reported in Perrett et al. (2010) were used to correct SN Ia distance moduli in SNLS 3-year cosmological analyses (Guy et al. 2010; Conley et al. 2011). The aim here is to check whether we can measure this bias directly from data and with an analysis completely independent from that used to define the 3-year SNLS cosmological sample.

To do so, ideally one would compare average distance moduli at a given redshift, measured from the identified subsample and from the whole photometric sample. Our statistical sample being limited, we compare Hubble diagram residuals in large

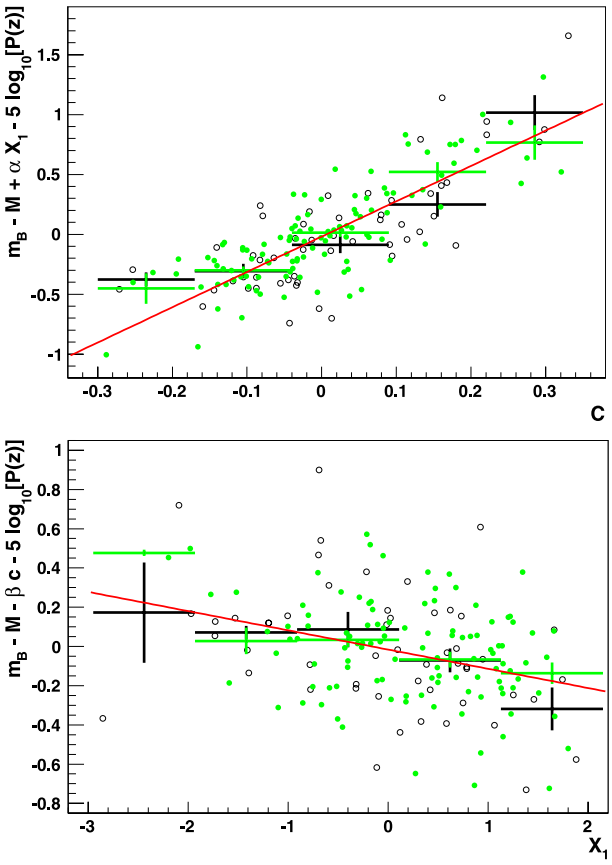


**Fig. 20.** Partial Hubble diagram residuals (and profiles) as a function of colour (*top*) and $X_1$ (*bottom*) for the identified (green filled circles and profiles) and unidentified (black open circles and profiles) subsamples of photometrically selected SNe Ia with $i_M < 23$. The straight lines are linear fits to the full sample of events with $i_M < 23$.

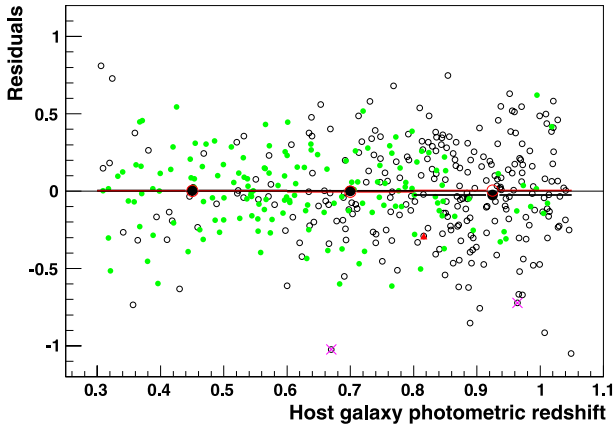


**Fig. 21.** Hubble diagram residuals. Green dots stand for the identified SN Ia subsample and open black circles for the unidentified subsample. Means are shown in three redshift bins, black for identified events, red for full sample. The red upward triangle is event SNLS 06D2bo which was erroneously typed as a possible core-collapse supernova initially (see Sect. 4.2 for details). The pink crosses mark the two $3\sigma$ outliers, which were excluded in the computation of the means.

bins of redshifts instead of distances at given redshift values. As all events were submitted to the same selection procedure and the same redshift assignment, such a comparison is directly sensitive to different Malmquist biases and should not be altered by systematic uncertainties related to data processing.

The residuals of the Hubble diagram are presented in Fig. 21 for the two samples. The residuals were again defined from the distance moduli in Eq. (2) by subtracting $5\log[P(z)]$ where $P(z)$ is the third-order polynomial introduced in the previous section. The Hubble diagram residuals were then averaged in three large redshift bins, [0.3−0.6], [0.6−0.8] and [0.8−1.05], where both identified and unidentified samples had enough events to allow a quantitative comparison. In the computation of the means, $3\sigma$ outliers were rejected.

Mean values of the residuals (each weighted by the inverse of its variance) are reported in Table 7. The variance on each point includes both a contribution from the light curve fit and one from the use of a photometric redshift. For the latter, we used a typical redshift uncertainty of $\delta_z = 0.05$, that we translated into a distance modulus uncertainty using the derivative of the cosmological model introduced in Sect. 3.3.1. By construction, the residuals of the total sample are 0 (see also Fig. 21). The last line of Table 7 gives the difference between the mean residuals in the identified and total samples, which directly measures the mean difference in distance modulus between the two samples, $\Delta\mu_{\rm id}$.

Up to a redshift of 0.8, distance moduli in the identified and the total samples do not exhibit significant differences. In the last redshift bin, corresponding to a mean redshift of 0.9, distance moduli in the two samples have an average offset of $\Delta\mu_{\rm id} = -0.030 \pm 0.036$ (stat.). This result is stable with respect to different redshift binning or outlier cuts.

### 5.3. Offset correction and systematics

As shown in Fig. 22, the bias towards selecting bluer, and hence brighter events at high redshift is clear in the identified sample and attenuated in the photometric sample. Although the latter effect may be due to evolution of Type Ia supernovae, it can also result from selection effects (our photometric sample being magnitude limited and biased against SNe in faint host galaxies). In that case, the offset value quoted in the previous section should be corrected for the incompleteness of the photometric sample. A correction for the residual core-collapse contamination of the sample may also be needed.

These two corrections were determined from the synthetic supernova light curves, which were submitted to the same selections as data. Residuals were here computed w.r.t. the luminosity distance for the cosmology used in the simulation (see Sect. 3.3.1). In the redshift bin [0.80, 1.05], synthetic SNe Ia passing our photometric selection exhibit a negative average residual of $-0.0148 \pm 0.006(stat.)$, while the selected CC SNe (less than 1 event out of 191) contribute for a tiny residual of $+0.0005 \pm 0.0008(stat.)$. The offset of the photometric sample thus amounts to $\Delta\mu_{\rm phot} = -0.014 \pm 0.006(stat.)$ and the total offset of the identified subsample in the redshift interval $0.8 < z < 1.05$ is $\Delta\mu = \Delta\mu_{\rm id} + \Delta\mu_{\rm phot} = -0.044 \pm 0.036(stat.)$.

Systematic uncertainties due to the limited precision of redshift assignment and photometry may affect this result. These effects were again studied with the synthetic SN Ia light curves. Changes in the mean residuals of the photometric sample and its bright subsample are reported in Table 8. The difference between the residuals of the two samples compares directly with $\Delta\mu_{\rm id}$, while the mean residual of the photometric sample identifies with the correction term $\Delta\mu_{\rm phot}$. Table 8 shows that improving the redshift determination and the photometry precision leads to almost identical shifts of the mean residuals of the two samples. These two effects have therefore a negligible impact on the measurement of $\Delta\mu_{\rm id}$. The table also shows that the systematic

**Table 7.** Hubble diagram mean residuals for different samples of SN Ia data selected by this analysis.

| SN Ia sample | Mean residuals in redshift bins | | |
|---|---|---|---|
| | $0.3 < z < 0.6$ | $0.6 < z < 0.8$ | $0.8 < z < 1.05$ |
| Identified | $0.004 \pm 0.032$ (76) | $0.003 \pm 0.033$ (51) | $-0.025 \pm 0.041$ (31) |
| Unidentified | $-0.002 \pm 0.053$ (31) | $-0.009 \pm 0.032$ (67) | $0.013 \pm 0.022$ (160) |
| Total | $0.002 \pm 0.027$ (107) | $-0.003 \pm 0.023$ (118) | $0.005 \pm 0.019$ (191) |
| $\Delta\mu_{\rm id}$ = Identified – Total | $0.002 \pm 0.017$ | $0.006 \pm 0.024$ | $-0.030 \pm 0.036$ |

**Notes.** Host photometric redshifts were used for all events. The number of events in each bin is indicated in parenthesis. The last line shows the difference $\Delta\mu$ between the mean residuals in the identified and total samples. Uncertainties are statistical only.

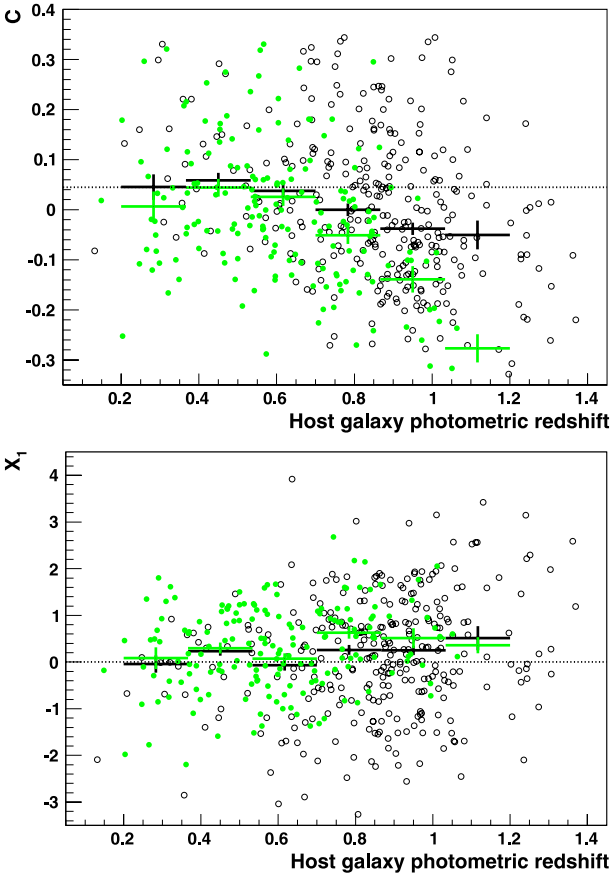


**Fig. 22.** Distributions of colour (*top*) and $X_1$ (*bottom*) as a function of the host galaxy photometric redshift, for the identified (green filled circles and profiles) and unidentified (black open circles and profiles) subsamples of photometrically selected SNe Ia.

**Table 8.** Effect of redshift and photometry resolutions on mean residuals.

| Analysis conditions | Mean residual | |
|---|---|---|
| | Bright SNe | Photometric SNe |
| This analysis | $-0.033 \pm 0.007$ | $-0.015 \pm 0.006$ |
| $\lvert\Delta z\rvert/(1+z) < 10\%$ | $-0.034 \pm 0.007$ | $-0.016 \pm 0.006$ |
| $\lvert\Delta z\rvert/(1+z) < 3\%$ | $-0.042 \pm 0.009$ | $-0.020 \pm 0.008$ |
| $\lvert\Delta z\rvert/(1+z) < 1\%$ | $-0.044 \pm 0.014$ | $-0.021 \pm 0.012$ |
| Perfect photom. & $z$ | $-0.043 \pm 0.007$ | $-0.024 \pm 0.006$ |
| Difference | $-0.010 \pm 0.009$ | $-0.009 \pm 0.008$ |

**Notes.** The table details the changes in the weighted mean residuals of the identified and photometric SN Ia samples, as expected if resolutions in redshift and photometry were gradually improved w.r.t. their values in the present analysis (first line). All changes were estimated from synthetic SN Ia light curves. Uncertainties are statistical.

uncertainty on $\Delta\mu_{\rm phot}$ is of order –0.01, negligible w.r.t. the statistical uncertainty of the method.

As previously mentioned, a precise determination of the magnitude offset in the SNLS 3-year spectroscopic sample was obtained in Perrett et al. (2010) with Monte Carlo simulations. The shift in the average magnitude of the spectroscopic sample towards brighter values was found to become significant for $z > 0.75$, rising from $-0.013 \pm 0.001(stat.)$ at $z \sim 0.8$ to $-0.038 \pm 0.003(stat.)$ at $z \sim 1.05$, with a systematic uncertainty of 20%. The result reported here, $\Delta\mu = -0.044 \pm 0.036(stat.) \pm 0.010(syst.)$ in the redshift interval $0.8 < z < 1.05$, obtained mostly from data and from an analysis independent from the real-time SNLS processing, agrees with the above values.

## 6. Conclusions

The SuperNova Legacy Survey offers one of the best data sets to test SN Ia photometric typing methods in the redshift range between 0.2 and 1.0. Although spectra remain essential to achieve the level of accuracy required in cosmology studies, many supernova studies such as rate measurements or correlations with host galaxy properties benefit from the larger statistics allowed by photometrically identified samples.

In this paper, the 3-year SNLS image sample was submitted to a deferred search for Type Ia supernovae based on their multi-colour light curves and an external catalogue of photometric redshifts of host galaxies. SN-like transient events were first selected using light curve shape criteria. The selected light curves were fitted under the assumption that the events were SNe Ia using SALT2 as light curve fitter. Selections were then designed to both discriminate SNe Ia against core-collapse ones and to assess the reliability of the redshift assignment. They were applied to the SALT2 fitted parameters, rest-frame $B-V$ colour, stretch-related $X_1$ parameter, as well as colours and magnitudes in the MegaCam filters. These selections allowed us to select a sample of 485 SN Ia events with host galaxy photometric redshifts.

The performance of the analysis was studied with synthetic light curves of Type Ia and core-collapse supernovae. The selection efficiency for bright SNe Ia with well sampled light curves is 80% in case a host galaxy photometric redshift is available. The contamination of the selected sample from other types of supernovae is 4%.

One third of the photometrically selected events have confirmed Ia types from SNLS spectroscopy. These events were compared with the rest of the photometric sample which has no or incomplete spectroscopic information. In the range of magnitudes allowed by spectroscopic identification, there is no significant differences in the intrinsic features of events with and without spectroscopic identification.

The higher magnitude limit of the whole photometric sample allowed distances derived from spectroscopically identified

events to be tested in order to measure the Malmquist bias due to spectroscopic sample selections, directly from data and with an analysis independent from the SNLS cosmological analyses. A magnitude offset was found at redshifts above 0.8, though with a large statistical uncertainty. The obtained offset is consistent with the more precise result derived from Monte Carlo simulations which was used to correct SN Ia distance moduli in the SNLS 3-year cosmological analyses.

This paper demonstrates the feasibility of a photometric selection of high redshift supernovae with known photometric host galaxy redshifts, opening interesting prospects for cosmological analyses from large photometric SN Ia surveys, as planned in the near future. In this respect, the points we found most important for such an analysis are the following. The cadence of observations must be chosen to obtain light curves with a temporal sampling of a few days. The number of filters must allow SN colours and magnitudes to be determined in a reliable way on the whole SN redshift range. A low contamination by core-collapse supernovae can be achieved when using photometric host galaxy redshifts with a few % resolution and rate of catastrophic redshifts, provided selections include enough criteria to reject events with incorrect redshift assignments.

*Acknowledgements.* SNLS is based on observations obtained with MegaPrime/MegaCam, a joint project of CFHT and CEA/Irfu, at the Canada-France-Hawaii Telescope (CFHT) which is operated by the National Research Council (NRC) of Canada, the Institut National des Sciences de l'Univers of the Centre National de la Recherche Scientifique (CNRS) of France, and the University of Hawaii. This work is based in part on data products produced at TERAPIX and the Canadian Astronomy Data Centre as part of the Canada-France-Hawaii Telescope Legacy Survey, a collaborative project of NRC and CNRS. This paper makes use of photometric redshifts produced jointly by TERAPIX and VVDS teams. SNLS also relies on observations obtained at the European Southern Observatory using the Very Large Telescope on the Cerro Paranal (ESO Large Programme 171.A-0486), on observations (programs GN-2006B-Q-10, GN-2006A-Q-7, GN-2005B-Q-7, GS-2005B-Q-6, GN-2005 A-Q-11, GS-2005A-Q-11, GN-2004B-Q-16, GS-2004B-Q-31, GN-2004A-Q-19, GS-2004A-Q-11, GN-2003 B-Q-9, and GS-2003B-Q-8) obtained at the Gemini Observatory, which is operated by the Association of Universities for Research in Astronomy, Inc., under a cooperative agreement with the NSF on behalf of the Gemini partnership: the National Science Foundation (United States), the Particle Physics and Astronomy Research Council (United Kingdom), the National Research Council (Canada), CONICYT (Chile), the Australian Research Council (Australia), CNPq (Brazil) and CONICET (Argentina), and on observations obtained at the W.M. Keck Observatory, which is operated as a scientific partnership among the California Institute of Technology, the University of California and the National Aeronautics and Space Administration. The Observatory was made possible by the generous financial support of the W. M. Keck Foundation. M.S. acknowledges support from the Royal Society.

## Appendix A: detection efficiency model

The detection efficiency for a supernova with date $t_{0i}$ of maximum light in $i_M$-band depends on its peak magnitude $m_{0i}$, on the seeing and sky background during nearby observing times $t_k$, and on the relative epochs $t_{0i} - t_k$. The dependence of the efficiency on these variables was studied with Monte Carlo images on D1.

As an example, the season-averaged average detection efficiency $\epsilon(m_{0i})$ is illustrated in Fig. A.1. On average over the CCD mosaic, all three seasons exhibit very similar efficiencies, except for CCD 3 which failed to work during three out of the six dark time periods of the first season. The efficiency is nearly magnitude-independent out to $m_{0i} = 23.5$ and then steeply declines at fainter magnitudes.

With varying observing conditions, we found that the efficiency as a function of magnitude had the form of the mean efficiency in Fig. A.1, but that the maximum efficiency and cutoff magnitude depended on conditions. The adopted efficiency model therefore has the form:

$$\epsilon(t_{0i}) = \epsilon_{\max}(t_{0i})\, F(m - m_c(t_{0i}))$$

where $F(m - m_c)$ is the mean of the functions shown in Fig. A.1 ($F(-m_c) = 1$ and $F(0) = 1/2$). The function $\epsilon_{\max}$ is the efficiency at bright magnitudes while $m_c$ is the magnitude at which the efficiency drops to $\epsilon_{\max}/2$. The $t_{0i}$ dependence of $\epsilon_{\max}$ and $m_c$ reflects the observing conditions near $t_{0i}$. It was found that they could both be determined by a single function $f(t_{0i})$:

$$\epsilon_{\max}(t_{0i}) = 1 - 0.2 f(t_{0i}) \qquad m_c(t_{0i}) = 25.3 - 5.4 f(t_{0i}). \tag{3}$$

The efficiency-loss function, $f(t_{0i})$, vanishes for the best observing conditions. It was taken to be a product over all lunations:

$$f(t_{0i}) = \prod_l [1 - \alpha(\boldsymbol{o}_l) \times \beta(\Delta t_l)] \tag{4}$$

where $\alpha$ is a function of the mean observing conditions, $\boldsymbol{o}_l = (seeing, \; sky \;\; background)$ for the lunation and $\beta$ is a function of the difference, $\Delta t_l$, between the time of supernova maximum light and the time of the nearest measurement. Figures A.2 and A.3 show the adopted functions. Note that for $\Delta t_l > 50$ days, $\beta(\Delta t_l) \to 0$, so in practice only the three lunations closest to the explosion determine $f(t_{0i})$. The impact of temporary CCD failures is automatically accounted for in this model by setting $\alpha(\boldsymbol{o}_l) = 0$ for non-working CCDs, leading to large intervals between the maximum light date $t_{0i}$ and the actual dates of observation, and hence to lower detection efficiencies.

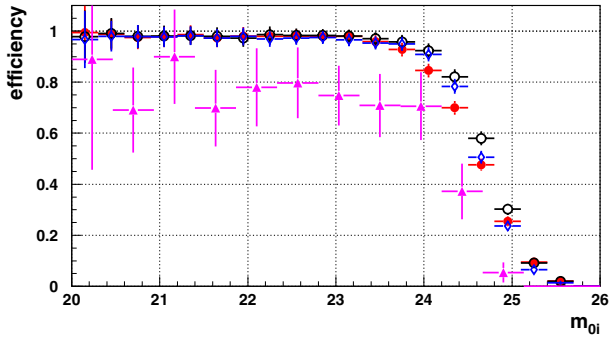


**Fig. A.1.** Detection efficiency $\epsilon(m_{0i})$ on D1 derived from Monte Carlo images as a function of the generated magnitude $m_{0i}$ at maximum light. Blue diamonds illustrate the efficiency for the first season of data (averaged over the full mosaic excluding CCD 3), red disks are for the second season (full mosaic), open black circles are for the third season (full mosaic), and pink triangles are for the supernovae occurring during the first season on CCD 3.

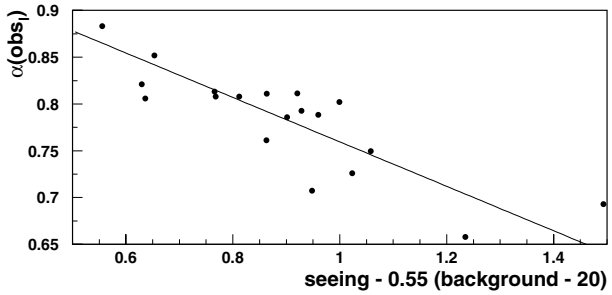


**Fig. A.2.** Lunation detection probabilities $\alpha(\boldsymbol{o}_l)$ from the D1 Monte Carlo as a function of mean lunation seeing (in arcsec) and background (in mag per arcsec$^2$). The line is the adopted $\alpha(\boldsymbol{o}_l)$.

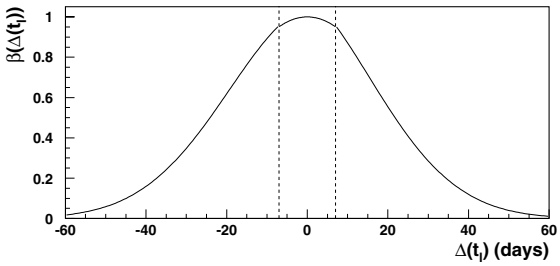


**Fig. A.3.** Analytical model of the temporal dependence $\beta(\Delta t_l)$, here illustrated for a fourteen-day lunation. Dashed lines indicate the lunation boundaries. The model consists of two decreasing exponentials outside the lunation boundaries (with a steeper decline for positive $\Delta t_l$ because the fall time of a SN Ia is larger than its rise time) and is roughly flat inside.

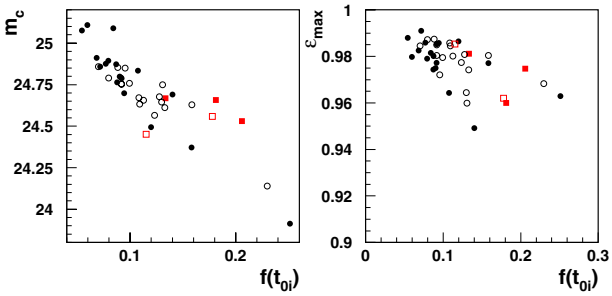


**Fig. A.4.** Correlations between the measured parameters ($m_c$ and $\epsilon_{max}$) and $f(t_{0i})$, as observed in the D1 Monte Carlo. Each point is an average over all $t_{0i}$ dates in a lunation (filled symbols) or inter-lunation period (open symbols). Circles are averaged over the full mosaic, except for the first season where CCD 3 has been singled out (red squares) due to intermittent failures. Linear fits are used in the model to describe the observed correlations.

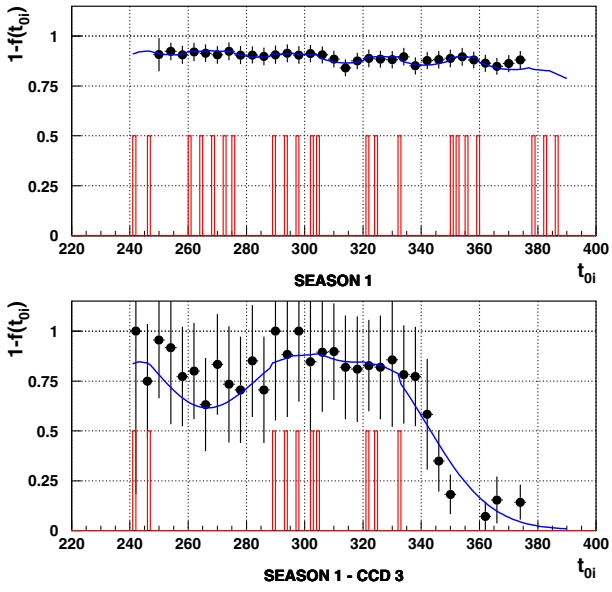


**Fig. A.5.** Temporal dependence of the detection efficiency, $1 - f(t_{0i})$, on D1, with dates originating at January 0, 2003. The model (blue curve) is compared with Monte Carlo estimates (black points). Actual observation dates are shown as the lower red histograms. The bottom plot is for CCD 3 which failed to work during the second and the last two lunations. The top plot is for the rest of the mosaic.

The linear dependence of $\epsilon_{max}$ and $m_c$ on $f(t_{0i})$ (see Eq. (3)) is illustrated in Fig. A.4. We see that the primary effect of degraded observing conditions is to lower the cutoff magnitude: conditions that degrade $m_c \sim 25$ to $m_c \sim 24$ change the efficiency for bright supernova only from $\epsilon_{max} \sim 0.98$ to $\epsilon_{max} \sim 0.96$. Note also that $m_c$ differs on average by about 0.25 mag for supernovae occurring during a lunation compared to those between lunations. The case of CCD 3 in the first season has been also singled out to show all cases of inter-lunation durations, from fifteen days (normal CCD working conditions) to over one month. Figure A.4 shows that the observed correlations can be described by the same linear fits, whether $t_{0i}$ occurred during a lunation or outside, for working CCDs or not.

Figure A.5 compares the model for $1 - f(t_{0i})$ (blue curve) with the $1 - f(t_{0i})$ derived directly from the Monte Carlo images (shown as the black points). There is a clear agreement between the two estimates. The model reproduces both the efficiency during the observation periods and the loss of efficiency between these, which varies with the duration of the absence of data. This is clearly emphasized in the bottom plot of Fig. A.5 where the temporary failures of CCD 3 enhance the efficiency loss due to lack of data.

## Appendix B: additional efficiency plots

This appendix gives the SN Ia photometric selection efficiency as a function of the generated SN Ia colour and $X_1$ (see Fig. B.1).

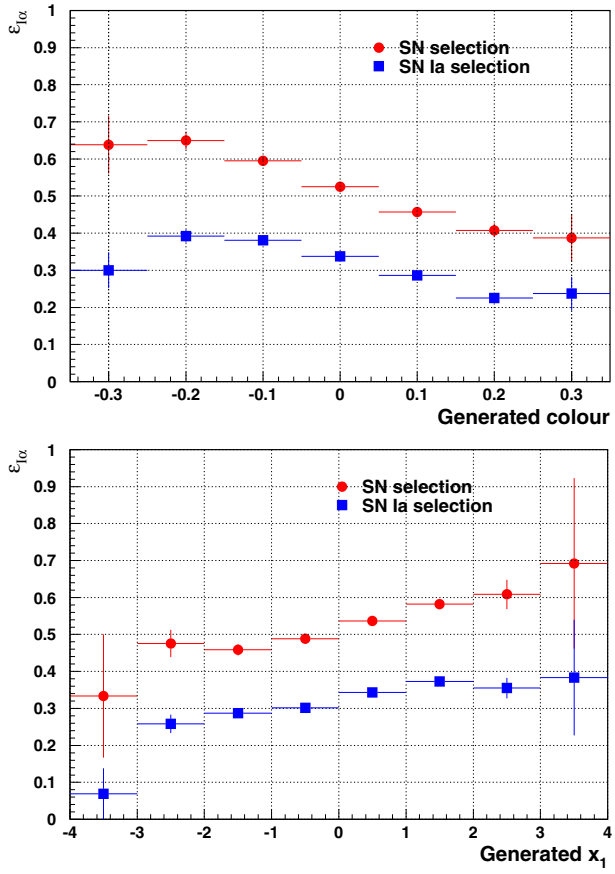


**Fig. B.1.** Selection efficiency from synthetic SN Ia light curves as a function of the generated colour and $X_1$, at different stages of the analysis.

## References


Alard, C., & Lupton, R. H. 1998, ApJ, 503, 325
Astier, P., Guy, J., Regnault, N., et al. 2006, A&A, 447, 31
Balland, C., Baumont, S., Basa, S., et al. 2009, A&A, 507, 85
Bazin, G. 2008, Ph.D. Thesis, Université Paris Diderot, Paris 7
Bazin, G., Palanque-Delabrouille, N., Rich, J., et al. 2009, A&A, 499, 653
Bertin, E. 2006, ASP Conf. Ser., 351, 112
Bertin, E., & Arnouts, S. 1996, A&AS, 117, 393
Bertin, E., Mellier, Y., Radovich, M., et al. 2002, ASP Conf. Ser., 281, 228
Boulade, O., Charlot, X., Abbon, P., et al. 2003, in Instrument Design and Performance for Optical/Infrared Ground-based Telescopes, ed. M. Iye, A. F. M. Moorwood, Proc. SPIE, 4841, 72
Bronder, T. J., Hook, I. M., Astier, P., et al. 2008, A&A, 477, 717
Cardelli, J. A., Clayton, G. C., & Mathis, J. S. 1989, ApJ, 345, 245
Conley, A., Guy, J., Sullivan, M., et al. 2011, ApJS, 192, 1
Ellis, R. S., Sullivan, M., Nugent, P. E., et al. 2008, ApJ, 674, 51
Frieman, J. A., Bassett, B., Becker, A., et al. 2008, AJ, 135, 338
González-Gaitán, S., Perrett, K., Sullivan, M., et al. 2011, ApJ, 727, 107
Guy, J., Astier, P., Baumont, S., et al. 2007, A&A, 466, 11
Guy, J., Sullivan, M., Conley, A., et al. 2010, A&A, 523, A7
Hopkins, A. M., & Beacom, J. F. 2006, ApJ, 651, 142
Howell, D. A., Sullivan, M., Perrett, K., et al. 2005, ApJ, 634, 1190
Howell, D. A., Sullivan, M., Nugent, P. E., et al. 2006, Nature, 443, 308
Howell, D. A., Sullivan, M., Conley, A., & Carlberg, R. 2007, ApJ, 667, L37
Ilbert, O., Arnouts, S., McCracken, H. J., et al. 2006, A&A, 457, 841
Kessler, R., Bassett, B., Belov, P., et al. 2010, PASP, 122, 1415
Le Guillou, L. 2003, Ph.D. Thesis, Université Pierre et Marie Curie, Paris 6
Magnier, E. A., & Cuillandre, J.-C. 2004, PASP, 116, 449
Miknaitis, G., Pignata, G., Rest, A., et al. 2007, ApJ, 66, 674
Monet, D., Levine, S., Canzian, B., et al. 2003, ApJ, 125, 984
Palanque-Delabrouille, N., Ruhlmann-Kleider, V., Pascal, S., et al. 2010, A&A, 514, A63
Perlmutter, S., Aldering, G., Goldhaber, G., et al. 1999, ApJ, 517, 565
Perrett, K., Balam, D., Sullivan, M., et al. 2010, AJ, 140, 518
Pritchet, C. J., Howell, D. A., & Sullivan, M. 2008, ApJ, 683, L25
Regnault, N., Conley, A., Guy, J., et al. 2009, A&A, 506, 999
Riess, A. G., Filippenko, A. V., Challis, P., et al. 1998, AJ, 116, 1009
Ripoche, P. 2007, Ph.D. Thesis, Université de Marseille
Schlegel, D. J., Finkbeiner, D. P., & Davis, M. 1998, ApJ, 500, 525
Sullivan, M., Howell, A., Perrett, K., et al. 2006a, AJ, 131, 960
Sullivan, M., Le Borgne, D., Pritchet, C. J., et al. 2006b, ApJ, 648, 868
Sullivan, M., Conley, A., Howell, D. A., et al. 2010, MNRAS, 406, 782
Walker, E. S., Hook, I. M., Sullivan, M., et al. 2010, MNRAS, 410, 1262